

# UC Berkeley

## UC Berkeley Previously Published Works

### Title

A study of deformation and strain induced in bulk by the oxide layers formation on a Fe-Cr-Al alloy in high-temperature liquid Pb-Bi eutectic

### Permalink

<https://escholarship.org/uc/item/2x2513c5>

### Authors

Popovic, MP  
Chen, K  
Shen, H  
[et al.](#)

### Publication Date

2018-06-01

### DOI

10.1016/j.actamat.2018.03.041

Peer reviewed

Manuscript Number: A-17-3415R1

Title: A study of deformation and strain induced in bulk by the oxide layers formation on a Fe-Cr-Al alloy in high-temperature liquid Pb-Bi eutectic

Article Type: Full length article

Keywords: Laue X-ray microdiffraction; strain; oxidation; thermal constriction; FeCrAl alloy

Corresponding Author: Mr. Miroslav Popovic,

Corresponding Author's Institution:

First Author: Miroslav Popovic

Order of Authors: Miroslav Popovic; Kai Chen; Hao Shen; Camelia Stan; David Olmsted; Nobumichi Tamura; Mark Asta; Manuel Abad; Peter Hosemann

Abstract: At elevated temperatures, heavy liquid metals and their alloys are known to create a highly corrosive environment that causes irreversible degradation of most iron-based materials. It has been found that an appropriate concentration of oxygen in the liquid alloy can significantly reduce this issue by creating a passivating oxide scale that controls diffusion, especially if Al is present in Fe-based materials (by Al-oxide formation). However, the increase of the temperature and of oxygen content in liquid phase leads to the increase of oxygen diffusion into bulk, and to promotion of the internal Al oxidation. This can cause a strain in bulk near the oxide layer, due either to mismatch between the thermal expansion coefficients of the oxides and bulk material, or to misfit of the crystal lattices (bulk vs. oxides). This work investigates the strain induced into proximal bulk of a Fe-Cr-Al alloy by oxide layers formation in liquid lead-bismuth eutectic utilizing synchrotron X-ray Laue microdiffraction. It is found that internal oxidation is the most likely cause for the strain in the metal rather than thermal expansion mismatch as a two-layer problem.

Dear Sir,

I re-submit our paper entitled: "**A study of deformation and strain induced in bulk by the oxide layers formation on a Fe-Cr-Al alloy in high-temperature liquid Pb-Bi eutectic**" on behalf of all co-authors to Acta Materialia, after addressing all the revisions stated by the reviewer. In the study, we analyze a strain in the near-interface bulk of ferritic FeCrAl alloy after its exposure to heavy liquid metals. Two possible origins of strain were considered: internal oxidation of aluminum in bulk, and thermal expansion mismatch between the oxide and the bulk. A positive correlation of dislocation density with peak width distribution indicates that strain comes from plastic deformation, while the evidence of grain refinement and sub-grain formation indicates a noticeable internal oxidation. Based on the comparison with theoretical predictions, we conclude that internal oxidation is more dominant mechanism of strain induction.

Sincerely,

Miroslav P. Popovic,

UC Berkeley

We thank the reviewer for his/her time and effort.

Below we address all reviewer's comments (labeled "C") in detail, marked in green (labeled "A").

C 0: - Dear authors, congratulations for this interesting work.

A 0: We thank the reviewer for his/her assessment of our paper.

C1-1: You are studying the deformation and strain induced in the bulk of a Fe-Cr-Al alloy (Alkrothal 720) by oxide scales that form in liquid LBE. Alkrothal is a bcc alloy, a fact that you should clearly mention when you describe the material in the Experimental section (not just mention that it is a ferritic alloy), giving some basic information on the lattice parameters.

A1-2: We thank the reviewer for this suggestion. We made changes in the manuscript and modified our statement (in the first paragraph of section 2. Experimental), so it reads now as following:

*Alkrothal 720 (ALK), a ferritic iron-chromium-aluminum BCC alloy with high thermal and corrosion resistivity (lattice constant  $a = (2.866 \pm 0.001) \text{ \AA}$ , and composition provided by the vendor (Sandvik) [71]: 12-14% Cr, 4.0% Al (nominal), 0.7% Mn (max.), 0.7% Si (max.), 0.25% Ti (max.), and 0.08% C (max.) by weight with the balance of Fe), was exposed to liquid LBE at  $(800 \pm 5) \text{ }^\circ\text{C}$  for  $(360 \pm 1) \text{ h}$  in an in-house designed experimental setup in controlled oxygen atmosphere ( $\sim (5.0 \pm 0.5) \times 10^{-6} \text{ wt\%}$  oxygen in LBE, monitored by oxygen sensor), according to the test procedure described in previous work [19].*

C1-2. What you neglect to mention, however, is that ferritic/martensitic and ODS steels (all of which typically have the bcc structure) are extremely susceptible to liquid metal embrittlement (LME) in contact with LBE; therefore, they cannot be used as structural materials in LBE-cooled reactors (or in other applications that use LBE or other Pb-alloy coolants). Even if you argue that LME is suppressed at high temperatures, you cannot prevent your materials from undergoing regular thermal cycling through the temperature range of maximum LME (typically, in the 300-400 °C range), hence you cannot rely on the use of materials that might suffer catastrophic failure during service. Taking into account the prestige and influence of your academic establishment, I would strongly recommend that you do not let the readers of Acta to believe that it would be safe to use unprotected ferritic or ferritic/martensitic alloys as structural materials in LBE-cooled reactors or even in other applications where LBE is used as coolant; or that it would be preferable to use such alloys over austenitic stainless steels based solely on liquid metal corrosion arguments. Please alert the readers on the underlying danger of LME and provide a set of relevant references.

A1-2: We thank the reviewer for this suggestion. We added the following two sentences into the first paragraph of 1. Introduction in the manuscript:

*Besides the above mentioned phenomena, applying stress to the unprotected solid metals exposed to liquid metals, the former may experience liquid metal embrittlement (LME), characterized by premature brittle failure, depending on various parameters [72, 73]. At lower and higher temperatures, LME is less of an issue, leading to a temperature interval ("ductility*

*trough”) wherein the material is susceptible to LME (typically in 300 – 450 C range, for ferritic and ferritic-martensitic alloys) [74-76].*

C2: What is rather surprising is the fact that you perform a very advanced material characterization involving synchrotron X-ray Laue microdiffraction and you neglect the basic characterization of your LBE-oxidized alloy. Even though I personally find very interesting the new perspectives that this technique opens for sub-oxide steel/alloy characterization (at least to the labs that have this technique available) and the light it could shed on sub-oxide alloy deformation with all consequences on the alloy performance, the average reader - including the liquid metal corrosion expert for that matter - would like to see at least one SEM micrograph of the oxide scale that is discussed in your manuscript. My recommendation is the following:

(a). If you intend to maintain the focus of your work on this particular system, please add at least one SEM micrograph + one EDS line scan to characterize the oxide scale that formed in contact with LBE during this short-term (360 h) exposure to LBE. Your oxide is thick enough (10-15  $\mu\text{m}$ ) to allow for SEM/EDS characterization. This micrograph could become a combined figure with Fig. 1, if you do not want to increase the total number of figures. By performing a basic characterization of the oxide scale, you also do not have to speculate at the end of the article what the strain would be, if the oxide was  $\text{Fe}_3\text{O}_4$  or  $\text{Al}_2\text{O}_3$ , and would make it easier for you to draw firm conclusions.

(b). If you want to give to this study a more general applicability associated with the versatility of the employed technique and the possible conclusions one might draw by considering a limited set of data, you could shift the focus of your work on the material characterization technique and the opportunities it gives, and use your system (alloy, exposure conditions) as a test case. You could then either discuss the technique and its limitations by considering more than one oxidized specimens (e.g., either from the same alloy and exposed for various times and see how the analysis evolves as function of the oxide thickness, or from more than 1 alloys with different oxide scale configurations). You could also first present a theoretical treatment of the possible oxide scales and then confirm the validity of your theoretical predictions with conventional materials characterization techniques that are available in your lab (SEM/EDS, TEM). I am sure you could find the right perspective to present this study, if you choose to focus on the technique rather than on the specific system. In both cases (a) and (b), SEM/EDS micrographs with basic characterization of the studied systems are required in support of the synchrotron X-ray Laue microdiffraction findings.

A2: We thank the reviewer for this suggestion. We chose the first proposed approach for suggested improvement in the manuscript. Therefore the existed Figure 1 is renamed into Figure 1.a, and completed/supplied with additional two images: one SEM micrograph (Figure 1.b) plus one EDS line scan (Figure 1.c) of the oxide scale (formed on Fe-Cr-Al sample after exposure to LBE) that were added. Please, find them in the separate document that contains all the figures included in the submitted manuscript.

We also changed the last sentence in the first paragraph of section 2 - Experimental, by adding a short description of the performed SEM+EDS analysis procedure, so that there is now the following statement in the manuscript (the last sentence of the first paragraph in Experimental section):

*Cross-sectioned ALK sample was polished first down to 1200 grid by SiC paper followed by diamond suspension and 0.3  $\mu\text{m}$   $\text{Al}_2\text{O}_3$  solution (given in detail in ref. [19]), then analyzed by Quanta 3D field emission gun (FEG) scanning electron microscope equipped with energy-dispersive X-ray spectrometer “Oxford instruments”, ~ 15 hours after the end of the corrosion test.*

The following statement that describes the results of SEM+EDS analysis was added as the initial paragraph in the section 3 (Results):

*Scanning electron microscopy (SEM) with energy-dispersive X-ray spectrometry (EDS) analysis revealed a complex, multi-layer structure of oxide scale (Figure 1 b-c) of a total thickness of 10-15  $\mu\text{m}$ . Closest to the steel, a layer consisting of mostly Al-oxide (~ 5  $\mu\text{m}$ ) has been detected, followed by a Fe-Cr(-Al)-oxide (~ 6  $\mu\text{m}$ ), and then another one mostly-Al-oxide layer (~ 4  $\mu\text{m}$ ) closest (next) to the LBE (Fig. 1c). Localized discontinuities in the inner Al-oxide layer have been found, as well as the traces of Pb and Bi within the outer Al-oxide (the latter contributing to the difference in contrast observed in the SEM images, as in Fig. 1b).*

C2-1: Another interesting question you might want to address is what would happen if the oxide scale is a dual oxide (very common in steels, both ferritic/martensitic and austenitic, oxidized in LBE)? How would this affect the treatment you present at the end of the Discussion section?

A2-1: The case of dual (or mixed) oxide has been considered and discussed in the following statements (and treatment) added at the very end of the Discussion section:

*In case of mixed oxide, or multi-layer scale (as it is the real case, at least in this study), the contribution of resulting strains,  $A = (\varepsilon_{\text{Fe}_3\text{O}_4} - \varepsilon_{\text{ALK}})$  and  $B = (\varepsilon_{\text{Al}_2\text{O}_3} - \varepsilon_{\text{ALK}})$  has to be weighted (keeping in mind the different signs of the values in Eq. 4.8 and 4.9) to calculate the total resulting strain,  $\varepsilon_{\text{tot}}$ :*

$$\varepsilon_{\text{tot}} = xA + (1-x)B$$

*where  $x$  is an assessed percentage of magnetite in scale, based on EDS analysis results.*

C3: The plots in Fig. 7 are unreadable (numbers overlap, the background is too dark). I would recommend that you remove this figure or replace it with something more useful. Maybe it would suffice to describe the information you get on grain misorientation just in the text? You cannot expect the readers to draw conclusions from a figure they cannot even read (alternatively: put it in supporting material/appendix, if you consider it necessary and Acta allows this option).

A3: We removed Figure 7, as suggested, and slightly modified the text in the Discussion section to describe the information from that figure instead. The modified segment of the text now reads as following:

*For instance, at least 3 subgrains with similar but distinct orientations were indexed within one of the measurement spots located in the near-surface bulk zone. The misorientation between the two neighboring grains has been found to be about  $21.6^\circ$ , with the rotation axis roughly along the [011] axis of Grain 1the first one of them. The orientation of the third one is found to be even closer to the orientation of the first one, (with a tiny misorientation of only  $1.1^\circ$  between them), while the rotation axis is along the [101] direction of Grain 1the first one. The first and third*

*grain come from the same initial grain (the third one being a subgrain of the first one, with almost identical orientation), while the second one is an entirely newly-formed grain.*

After the removal of Figure 7, the figure previously labeled as Figure 8 now became Figure 7.

C4: What must be taken into account - and it is not commented upon in your text - is the time that elapsed between solidification, mounting of the sample and analysis. As you know very well, LBE undergoes a room temperature transformation that leads to expansion. This might lead to a change in the stress/strain state in your sample with time and might affect your results. Please clarify this aspect in your text (i.e., the time frame within which your data have been acquired after solidification). Also it would be better to rename the 'LBE precipitate' as 'solidified LBE residues' or just as 'LBE residues'.

A4: We thank the reviewer for this suggestion. We made changes in the manuscript and modified our statement (in the first and the second paragraph of the Experimental section), so it reads now as following:

*After the corrosion test, the sample was extracted from the liquid LBE (before solidification, at ~ 200 °C) while the test system was cooling down to room temperature, mounted in epoxy resin and subsequently cut in cross-section in the epoxy after ~ 12 h (time for epoxy resin to harden). This procedure ensures that the oxide layers are preserved as they appear on the material. Cross-sectioned ALK sample was polished first down to 1200 grid by SiC paper followed by diamond suspension and 0.3 μm Al<sub>2</sub>O<sub>3</sub> solution (given in detail in ref. [19]), then analyzed by Quanta 3D field emission gun (FEG) scanning electron microscope equipped with energy-dispersive X-ray spectrometer "Oxford instruments", ~ 15 hours after the end of the corrosion test.*

*Laue μXRD measurements were carried out ~ 23 h after the end of corrosion test, on Beamline 12.3.2 at the Advanced Light Source (ALS), Lawrence Berkeley National Laboratory [55].*

C4-1: Also it would be better to rename the 'LBE precipitate' as 'solidified LBE residues' or just as 'LBE residues'.

A4-1: We thank the reviewer for this suggestion. The term 'LBE precipitate' has been corrected/renamed as suggested, wherever it appeared in manuscript.

C5: Please provide the definition of the 'geometrically necessary dislocations (GNDs)' in your text. You also introduce twice the abbreviation GNDs in your text: in page 8 & page 9. Once is enough.

A5: We thank the reviewer for his/her suggestion. The following is added as the definition of geometrically necessary dislocations (and the abbreviation GNDs is now introduced only once in the text, as suggested, while the other one is removed):

*The anisotropic broadening indicates the existence of plastic deformation achieved by the geometrically necessary dislocations (GNDs), i.e. the dislocations exceeding in one sign (also called unpaired or polar dislocations) which occur due to the non-uniform plastic deformation accompanied by plastic strain gradients in material [70].*

C6: Replace the term 'deep' (page 8) with 'alloy bulk' or 'base alloy'.

A6: The suggested replacement has been applied.

C7: Replace the term 'disorientation' with 'misorientation' (page 9).

A7: The suggested correction (replacement) has been applied.

C8: It is unclear what you mean by the phrase 'the boundary is inhomogeneous, which is expected since it has a mixed metal/oxide interface'. Please explain: 'mixed' means 'an interface between dissimilar materials'?

A8: In order to clarify this statement, we modified it. It is now as follows:

*This suggests that the boundary is inhomogeneous, which indicates an intermittent protrusion of oxide phase into the bulk (in a form of internal oxidation).*

C9: Some improvement of the written English is still required. Sometimes, articles are missing (e.g., Abstract: "...of THE oxygen content in THE liquid phase..."), sometimes the text is grammatically incorrect (e.g., page 12: "One other (better ANOTHER) issue with this assumptionS...") or the wording could be improved (e.g., page 2: "... the efficient and nonreactive heat transfer fluids are essential PROPERTIES (instead of 'component')); page 9: "... the direction arrays of MAXIMUM and MINIMUM compression...").

A9: We thank the reviewer for these suggestions. All the suggested corrections have been done/applied in the text, exactly as recommended. Besides that, a thorough linguistic revision of the manuscript and improvement of the written English have been done as well.

1  
2  
3  
4 **A study of deformation and strain induced in bulk by the oxide layers**  
5  
6 **formation on a Fe-Cr-Al alloy in high-temperature liquid Pb-Bi eutectic**  
7  
8

9 M. P. Popovic<sup>1\*</sup>, K. Chen<sup>2\*</sup>, H. Shen<sup>2, 3</sup>, C. V. Stan<sup>3</sup>, D. L. Olmsted<sup>4</sup>, N. Tamura<sup>3</sup>, M. Asta<sup>4</sup>, M.  
10 D. Abad<sup>5</sup> and P. Hosemann<sup>1</sup>  
11

12  
13 <sup>1</sup>Department of Nuclear Engineering, University of California, Berkeley, CA 94720, USA

14 <sup>2</sup>Center for Advancing Materials Performance from the Nanoscale (CAMP-Nano), State Key  
15 Laboratory for Mechanical Behavior of Materials, Xi'an Jiaotong University, Xi'an, Shaanxi  
16  
17 710049, China  
18

19 <sup>3</sup>Advanced Light Source, Lawrence Berkeley National Laboratory, Berkeley, CA 94720, USA

20 <sup>4</sup>Department of Materials Science and Engineering, University of California, Berkeley, CA  
21 94720, USA  
22

23 <sup>5</sup>Instituto Quimico de Sarria, School of Engineering, University Ramon Llull, Barcelona, Spain  
24  
25

26  
27  
28  
29  
30  
31 **Abstract**  
32

33  
34 At elevated temperatures, heavy liquid metals and their alloys are known to create a highly  
35 corrosive environment that causes irreversible degradation of most iron-based materials. It has  
36 been found that an appropriate concentration of oxygen in the liquid alloy can significantly  
37 reduce this issue by creating a passivating oxide scale that controls diffusion, especially if Al is  
38 present in Fe-based materials (by Al-oxide formation). However, the increase of the temperature  
39 and of oxygen content in liquid phase leads to the increase of oxygen diffusion into bulk, and to  
40 promotion of the internal Al oxidation. This can cause a strain in bulk near the oxide layer, due  
41 either to mismatch between the thermal expansion coefficients of the oxides and bulk material,  
42 or to misfit of the crystal lattices (bulk vs. oxides). This work investigates the strain induced into  
43 proximal bulk of a Fe-Cr-Al alloy by oxide layers formation in liquid lead-bismuth eutectic  
44  
45  
46  
47  
48  
49  
50  
51  
52  
53  
54  
55  
56  
57  
58  
59

60 

---

  
61 \* Corresponding authors: [popovic@berkeley.edu](mailto:popovic@berkeley.edu), [kchenlbl@gmail.com](mailto:kchenlbl@gmail.com)  
62  
63  
64  
65

1  
2  
3  
4 utilizing synchrotron X-ray Laue microdiffraction. It is found that internal oxidation is the most  
5  
6 likely cause for the strain in the metal rather than thermal expansion mismatch as a two-layer  
7  
8 problem.  
9

## 10 11 12 **1. Introduction** 13 14

15  
16 Lead-bismuth eutectic (LBE: 44.5 wt% Pb, 55.5 wt% Bi) is an attractive alloy for use as  
17  
18 a fluid in heat storage and transport applications in nuclear and solar power generating systems  
19  
20 [1-4], due to its reduced melting point (123.5 °C), low viscosity, low reactivity, high thermal  
21  
22 conductivity and proper neutron yield [6-8]. In high power density systems, just as in nuclear  
23  
24 power and concentrated solar power systems are, an efficient and nonreactive heat transfer fluid  
25  
26 is an essential component. The limiting factors of thermal efficiency are the temperature at which  
27  
28 heat enters the engine and temperature of the environment where the heat is exhausted. In order  
29  
30 to achieve high thermal efficiency in these fluids, it is necessary to maintain the temperature  
31  
32 difference in the system, between the ‘cold leg’ (heat uptake) and ‘hot leg’ (heat delivery), at the  
33  
34 maximum possible. Since the minimum temperature in the system is limited by the melting point  
35  
36 of LBE, it is necessary to increase the hot-leg temperature as much as possible. However, a  
37  
38 major drawback in using liquid LBE at high temperatures elevation is the increasing solubility of  
39  
40 many chemical elements [3, 11, 13-16] and the potential for liquid-metal-assisted corrosion  
41  
42 (LME) of the structural materials in contact with LBE [5, 11-14]. Besides the above mentioned  
43  
44 phenomena, applying stress to the unprotected solid metals exposed to liquid metals, the former  
45  
46 may experience liquid metal embrittlement (LME), characterized by premature brittle failure,  
47  
48 depending on various parameters [72, 73]. At lower and higher temperatures, LME is less of an  
49  
50 issue, leading to a temperature interval (“ductility trough”) wherein the material is susceptible to  
51  
52 LME (typically in 300 – 450 C range, for ferritic and ferritic-martensitic alloys) [74-76]. These  
53  
54  
55  
56  
57  
58  
59  
60  
61

1  
2  
3  
4 issues can be mitigated or reduced by adding an appropriate amount of oxygen into liquid LBE  
5  
6 and keeping control of the oxygen concentration in order to form a protective oxide layer or  
7  
8 layers on or near the structural material surface [3, 17-19]. The oxidation of the elements from  
9  
10 liquid and solid phase depends on temperature, oxygen concentration and chemical potential  
11  
12 (Gibbs free energy change,  $\Delta G$ ) of oxidation. This is represented by the Ellingham diagram,  
13  
14 which enables visualization of whether the oxidation of a particular element is  
15  
16 thermodynamically possible or not at certain predefined conditions. This mechanism leads to the  
17  
18 use of structural alloys which should contain strong oxide formers with stable and diffusion-  
19  
20 limiting oxides.  
21  
22  
23  
24

25  
26 A significant number of studies on the formation of oxide layers in LBE at temperatures  
27  
28 above 450 °C have been performed on a variety of different steels, leading to theoretical models  
29  
30 of oxide formation proposed [20-26]. Austenitic (Fe-Cr-Ni) steels cannot be used at temperatures  
31  
32 > 550 °C because of the high solubility ( $S$ ) of nickel in lead and bismuth at these temperatures  
33  
34 ( $\log S_{Ni} = 1.53 - 873/T$ , for  $673 < T < 1173$  K) [28]. Therefore ferritic, ferritic-martensitic (F/M)  
35  
36 and oxide dispersion-strengthened (ODS) alloys are better candidates for such applications. It  
37  
38 has been shown that the addition of aluminum to the Fe-based ferritic materials is beneficial in  
39  
40 preventing corrosion attack and severe oxidation, by forming an Al-rich oxide layer [29-34]. A  
41  
42 thin but adherent  $Al_2O_3$  oxide layer provides an effective diffusion barrier for Fe, Cr, Pb and Bi  
43  
44 and protect the steel from heavy liquid metal attack [33-35]. 4-7 wt% of Al in addition to 12.5-17  
45  
46 wt% Cr are found to be sufficient to form an alumina layer in ferritic Fe-Cr-Al alloys at 400-750  
47  
48 °C, while lower Al concentrations (as well as higher Al if there is  $\leq 10$  wt% Cr) lead to the  
49  
50 formation of Fe- based spinel-type oxides,  $Fe_{3-x-y}Cr_xAl_yO_4$ , both in air and Pb/LBE [33, 34, 36].  
51  
52 Generally, the higher the Cr content present, the lower the Al content that is acceptable. Fe-Cr-Al  
53  
54  
55  
56  
57  
58  
59  
60  
61  
62  
63  
64  
65

1  
2  
3  
4 alloys display a so-called ‘third element effect’ (TEE), where Cr (having an oxygen affinity  
5  
6 intermediate between those of Fe and Al) is supposed to induce a transition between the internal  
7  
8 and external oxidation of Al on ternary alloys under lower Al levels than for binary Fe-Al alloys  
9  
10 [37-39]. The grown alumina scales are transient polymorphs that gradually transform into stable  
11  
12 alumina [40] implying a volumetric change of ~14% in transformation from  $\gamma$ -Al<sub>2</sub>O<sub>3</sub> into  $\alpha$ -  
13  
14 Al<sub>2</sub>O<sub>3</sub> [41]. Spinel oxides have low thermal conductivity, while magnetite (Fe<sub>3</sub>O<sub>4</sub>) is reported to  
15  
16  
17 tend to spall off [37, 42]. Spalling is reported also for Al<sub>2</sub>O<sub>3</sub> protective scales [19, 33, 34, 36 and  
18  
19  
20  
21 43].  
22  
23

24 While the oxide layers themselves have been subject to numerous studies, the interaction  
25  
26 between the oxide layer and the substrate alloy has received only limited attention. In case of  
27  
28 high temperatures and higher oxygen concentrations in LBE, the diffusion of oxygen through the  
29  
30 oxide layers and into the steel bulk can become significant and lead to internal oxidation of Al,  
31  
32 particularly along the grain boundaries [44]. Strain generation in the oxide and in near-oxide  
33  
34 bulk due to the mismatch between the crystal structures of the oxides in scale and of the bulk has  
35  
36  
37 been reported previously [45, 47]. This mismatch might be one of the reasons for the oxide  
38  
39 scales failure (breaking, spalling) that leads to the uncontrolled material dissolution/loss. The  
40  
41 influence of Cr content on the microstructure and interfacial adhesion of the oxide scale formed  
42  
43 on steel alloys has been investigated [46] and it was found that the Cr-oxide layers survived up to  
44  
45  
46 5% of the tensile strain, while the Cr content in oxide phase determines the adhesion strength of  
47  
48  
49 the scales. In addition, the thermal expansion coefficient mismatch between the oxides and the  
50  
51 bulk might also contribute to the oxide spalling, in cooling at the end of heat transfer systems  
52  
53  
54 operation. Abad et al. investigated the binding strength between the oxide layers and metals by  
55  
56  
57 using small scale mechanical testing [42], but the strain in the metal upon cooling of oxidized  
58  
59  
60  
61  
62  
63  
64  
65

1  
2  
3  
4 samples has not been evaluated. It may be responsible for breaking and spalling of oxide layers  
5  
6 especially if thermal cycling (as in solar thermal applications) is considered [47-51]. Therefore,  
7  
8 the crystal lattice misfit and the thermal expansion mismatch are complimentary features and can  
9  
10 both contribute to the oxide scales failure. The intention of this study is to examine what  
11  
12 mechanism might be the most dominant one in Fe-Cr-Al alloy, at the upper limit (“hot-leg”)  
13  
14 temperature of 800<sup>0</sup>C. In the study, we evaluate the micro-strain and distribution of plastic  
15  
16 deformation near the steel-oxide interface in a Fe-Cr-Al alloy by using synchrotron X-ray Laue  
17  
18 microdiffraction ( $\mu$ XRD). This proved to be an efficient method for correlation of mechanical  
19  
20 properties with local structure at micron scale [52-57].  
21  
22  
23  
24  
25  
26

## 27 **2. Experimental**

28  
29  
30 Alkrothal 720 (ALK), a ferritic iron-chromium-aluminum BCC alloy with high thermal  
31  
32 and corrosion resistivity (lattice constant  $a = (2.866 \pm 0.001) \text{ \AA}$ , and composition provided by the  
33  
34 vendor (Sandvik) [71]: 12-14% Cr, 4.0% Al (nominal), 0.7% Mn (max.), 0.7% Si (max.), 0.25%  
35  
36 Ti (max.), and 0.08% C (max.) by weight with the balance of Fe), was exposed to liquid LBE at  
37  
38 (800  $\pm$ 5) <sup>0</sup>C for (360  $\pm$ 1) h in an in-house designed experimental setup in controlled oxygen  
39  
40 atmosphere ( $\sim (5.0 \pm 0.5) \times 10^{-6}$  wt% oxygen in LBE, monitored by oxygen sensor), according to  
41  
42 the test procedure described in previous work [19]. 800<sup>0</sup>C was chosen as a projected upper-limit  
43  
44 operational temperature (beyond the temperatures previously used in LBE studies) for achieving  
45  
46 better thermal efficiency. 360 h is a half month (15 days) period, which was the maximum  
47  
48 permitted by the extent of the entire test matrix used in our wider research. Oxygen concentration  
49  
50 was chosen based on the Ellingham’s diagram as a near-minimum value needed for Fe-, Cr- and  
51  
52 Al- oxides formation while disabling oxidation of lead and bismuth. After the corrosion test, the  
53  
54 sample was extracted from the liquid LBE (before solidification, at  $\sim 200$  <sup>0</sup>C) while the test  
55  
56  
57  
58  
59  
60  
61  
62  
63  
64  
65

1  
2  
3  
4 system was cooling down to room temperature, mounted in epoxy resin and subsequently cut in  
5  
6 cross-section in the epoxy after ~ 12 h (time for epoxy resin to harden). This procedure ensures  
7  
8 that the oxide layers are preserved as they appear on the material. Cross-sectioned ALK sample  
9  
10 was polished first down to 1200 grid by SiC paper followed by diamond suspension and 0.3  $\mu\text{m}$   
11  
12  $\text{Al}_2\text{O}_3$  solution (given in detail in ref. [19]), then analyzed by Quanta 3D field emission gun  
13  
14 (FEG) scanning electron microscope equipped with energy-dispersive X-ray spectrometer  
15  
16 “Oxford instruments”, ~ 15 hours after the end of the corrosion test.  
17  
18  
19  
20  
21

22 Laue  $\mu\text{XRD}$  measurements were carried out ~ 23 h after the end of corrosion test, on  
23  
24 Beamline 12.3.2 at the Advanced Light Source (ALS), Lawrence Berkeley National Laboratory  
25  
26 [55]. A schematic of the Laue diffraction setup and the details are given in Ref. [56]. The sample  
27  
28 was mounted on a high resolution x–y scanning stage with its polished cross-section facing up, at  
29  
30 a  $45^\circ$  tilt angle relative to the incident X-ray beam. Prior to XRD scan, a fast X-ray fluorescence  
31  
32 (XRF) scan was conducted using a Si drift detector to position the sample edge (to ensure that all  
33  
34 diffraction scans cover the desired region) and detect the expected elements in the scanned  
35  
36 region. A polychromatic X-ray beam (5–24 keV) was focused by a pair of Kirkpatrick–Baez  
37  
38 (KB) mirrors to  $\sim 1 \times 1 \mu\text{m}^2$  at the full width half maximum of the beam. Measurements were  
39  
40 conducted in the near-surface region that includes the oxide layer over a  $100 \times 50 \mu\text{m}^2$  area, as  
41  
42 shown in Figure 1a.  
43  
44  
45  
46  
47  
48

49 The diffraction scanning step size was 1  $\mu\text{m}$ , and a Laue pattern was recorded at each step with 1  
50  
51 s exposure time using an area DECTRIS Pilatus 1M detector which was placed about 140 mm  
52  
53 away from the X-ray focal point at  $90^\circ$  with respect to the incoming beam. The diffraction  
54  
55 geometrical parameters including sample-to-detector distance, center channel position and tilt of  
56  
57 the detector were calibrated by indexing a Laue diffraction pattern taken from a strain free sharp  
58  
59  
60  
61  
62  
63  
64  
65

1  
2  
3  
4 diffraction pattern within the sample far from the interface of the specimen using an in-house  
5 developed software XMAS [57]. Then all the 5000 recorded Laue patterns were automatically  
6 indexed using XMAS to obtain the crystal orientation and lattice strain at each scanning position.  
7  
8 This technique provides high resolution of both crystal orientation ( $0.01^\circ$ ) [58] and of deviatoric  
9 strain ( $\sim 10^{-4}$ ) [59], while the defect type and density distribution in the scan area can also be  
10 revealed from the shape of the diffraction peaks [60-61].  
11  
12  
13  
14  
15  
16  
17  
18

### 19 **3. Results**

20  
21  
22 Scanning electron microscopy (SEM) with energy-dispersive X-ray spectrometry (EDS)  
23 analysis revealed a complex, multi-layer structure of oxide scale (Figure 1 b-c) of a total  
24 thickness of 10-15  $\mu\text{m}$ . Closest to the steel, a layer consisting of mostly Al-oxide ( $\sim 5 \mu\text{m}$ ) has  
25 been detected, followed by a Fe-Cr(-Al)-oxide ( $\sim 6 \mu\text{m}$ ), and then another one mostly-Al-oxide  
26 layer ( $\sim 4 \mu\text{m}$ ) closest (next) to the LBE (Fig. 1c). Localized discontinuities in the inner Al-oxide  
27 layer have been found, as well as the traces of Pb and Bi within the outer Al-oxide (the latter  
28 contributing to the difference in contrast observed in the SEM images, as in Fig. 1b).  
29  
30  
31  
32  
33  
34  
35  
36  
37  
38

39 Two maps of  $50 \times 100$  pixels are generated from the  $\mu\text{XRD}$  patterns, as described  
40 elsewhere [55]: recorded intensity map (RIM) and filtered intensity map (FIM). In the RIM, four  
41 different zones are visible (Figure 2a): besides the epoxy-holder region which is the lowest-  
42 intensity one, the next lowest intensity one is the low-ordered (phase-transformed) region that  
43 corresponds to the oxide phase grown atop the steel surface (10-15  $\mu\text{m}$ , in the center), while to  
44 the right is the zone of Pb-Bi residues ( $\sim 25 \mu\text{m}$ ) above the oxide scale (with structural elements  
45 dissolved in it) and furthest one is zone of epoxy, while to the left is the best-ordered (the  
46 brightest zone), the bulk steel crystal. The FIM image (Figure 2b) is obtained by adding a filter  
47 of four times of the average intensity of each pattern to qualitatively map the defect density and  
48  
49  
50  
51  
52  
53  
54  
55  
56  
57  
58  
59  
60  
61  
62  
63  
64  
65

1  
2  
3  
4 grain boundaries, so the bulk Fe-Cr-Al steel substrate, which is almost a single crystal, is visible,  
5  
6 while the rest (phase-transformed zones of oxide and solidified Pb-Bi residues) is mostly dark on  
7  
8 the image, with only traces from LBE residues still remaining a bit lighter in the dark  
9  
10 background. Comparing the two intensity maps as shown in Figures 2a and 2b (FIM and RIM),  
11  
12 allows to clearly distinguish between the steel, the oxide and the LBE zones (phases).  
13  
14

15  
16 After filtering ( $\geq 6$  peaks indexed), the crystal orientation at all scanning positions of the  
17  
18 remained area relative to the arbitrarily chosen [001] direction has been obtained. A slight  
19  
20 variation (deviation) of up to  $0.2^\circ$  in orientation of the segments of the steel crystal has been  
21  
22 found close to the interface (with a minimum detectable change of  $0.01^\circ$ , being the error  
23  
24 magnitude), so the orientation map is represented in a narrow range of  $26.7^\circ - 27.0^\circ$  (Figure 2c),  
25  
26 with a complementary misorientation map (Figure 2d) obtained by comparing the orientation  
27  
28 matrix of each adjacent pair of scanning pixels, following the method introduced elsewhere [62].  
29  
30 This uncovers the fine orientation differences that represent possible plastic deformation and  
31  
32 defect formation.  
33  
34  
35  
36  
37  
38

39  
40 The peak width is defined as the average full width at half maximum (FWHM), in the  
41  
42 unit of degrees, of all indexed reflections in each Laue diffraction pattern. The peak width  
43  
44 increases and becomes significantly broadened in the region close to the metal/oxide interface  
45  
46 within the steel, concurrent with a decrease in observed peak intensity. The average peak width  
47  
48 evolution has been tracked along three lines parallel to the longer edge of XRD scan spot, i.e.  
49  
50 varying the X-coordinate (red, black and yellow lines in Figure 3a) and plotted in Figure 3b.  
51  
52 These line scans reveal a monotonic, uniform broadening (peak width increase).  
53  
54  
55  
56

57  
58 In order to reveal the mechanism that produces peak broadening, quantitative peak shape  
59  
60 analysis is performed on the  $(0\bar{1}3)$  peak, which was chosen because it was the most intense peak  
61  
62

1  
2  
3  
4 observed. Peak width has been measured by fitting the intensity with Lorentzian distribution  
5  
6 function, so that the width was determined with a precision of  $\sim 0.1$  pixels. The FWHM of the  
7  
8 peak in chosen spots increases as we go from the bulk towards the steel-oxide interface (Figures  
9  
10 3c-e). There is a slight change in crystal orientation detected near the interface (crystal  
11  
12 misorientation) that comes after the onset of increase in peak width as we move from the deep  
13  
14 towards the proximal bulk zone. This indicates a subgrains generation in a tiny zone of  
15  
16 orientation changes, narrower than the zone of plastic deformation (peak broadening). The  
17  
18 anisotropic broadening indicates the existence of plastic deformation achieved by the  
19  
20 geometrically necessary dislocations (GNDs), i.e. the dislocations exceeding in one sign (also  
21  
22 called unpaired or polar dislocations) which occur due to the non-uniform plastic deformation  
23  
24 accompanied by plastic strain gradients in material [70]. For simplicity, a typical  $(0\bar{1}3)$  peak has  
25  
26 been chosen and analyzed from the three co-linear spots (along the same line, parallel to the X-  
27  
28 coordinate: see red dots b - d on Figure 4a) and distanced  $35\ \mu\text{m}$ ,  $15\ \mu\text{m}$  and  $7\ \mu\text{m}$  respectively  
29  
30 (on the X-axis) from the oxide interface. The diffraction peak evolution has been monitored and  
31  
32 peak shape (dimensions) in the X-Y plane/projection has been analyzed (Figure 4, b - d). While  
33  
34 moving from alloy bulk towards the steel-oxide interface (along X-axis), there is a peak  
35  
36 streaking in more than one direction detected, which indicates the activation of more than one  
37  
38 dislocation slip systems. The tiny sharp peaks next to the main peak (circled, to the right, on  
39  
40 Figure 4d) appear with every Fe peak in the selected pattern, indicating the appearance of a well-  
41  
42 crystallized subgrain with slight rotation from the original matrix. However, it is not present in  
43  
44 every pattern along the boundary zone. This suggests that the boundary is inhomogeneous, which  
45  
46 indicates an intermittent protrusion of oxide phase into the bulk (in a form of internal oxidation).  
47  
48  
49  
50  
51  
52  
53  
54  
55  
56  
57  
58  
59  
60  
61  
62  
63  
64  
65

1  
2  
3  
4 Diffraction peak broadening is correlated to the defect density in a specimen according to  
5  
6 Barabash et al. [63] and Maaß et al. [64]. Streaking of Laue diffraction peaks can be linked to the  
7  
8 density of GNDs. For the crystal lattice parameter of BCC iron  $a = (2.866 \pm 0.001) \text{ \AA}$ , the  
9  
10 Burgers vector is  $b = \frac{1}{2} \cdot \langle 111 \rangle = a \cdot \frac{\sqrt{3}}{2} \approx 2.4825(9) \text{ \AA}$ , and the error is obtained as  $\Delta b =$   
11  
12  $\Delta a \cdot (b/a)$ . Dislocation density ( $\rho_D$ ) is calculated from the Cahn-Nye relation [65] as  $\rho_D = 1/(R \cdot b)$ .  
13  
14 Here,  $1/R$  is obtained as the lattice misorientation (in radians) per size of the scanned surface  
15  
16 element (which is  $1 \text{ \mu m}$ , same in both X and Y directions), i.e. as the angular difference in crystal  
17  
18 orientation between the two neighboring scanned surface elements, having the unit of  $\text{rad}/\mu\text{m}$ .  
19  
20 Therefore, the dislocation density map is obtained from the orientation map. The error  
21  
22 (uncertainty) of  $1/R$  values corresponds to the misorientation gradient that is  $0.01^\circ/\mu\text{m}$ . The  
23  
24 maximum GND density reaches the values of  $\sim 2 \times 10^9 \text{ cm}^{-2}$  (Figure 5). The dislocation density  
25  
26 is significantly higher (at least 10 times) at some spots in the proximity of steel-oxide interface  
27  
28 ( $\leq 10 \text{ \mu m}$  depth from the interface), compared to the values in the deep bulk zone, and stays in a  
29  
30 good correlation with the peak broadening zone (Figure 3a).  
31  
32  
33  
34  
35  
36  
37  
38  
39  
40

41 The strain tensor has been calculated using the formalism described in [66]. The principal  
42  
43 strain direction is calculated as the eigenvector of the deviatoric strain tensor, i.e. the three  
44  
45 eigenvectors and eigenvalues associated with the second order deviatoric strain tensor have been  
46  
47 calculated [67]. The magnitude of the eigenvector is the corresponding eigenvalue (where the  
48  
49 magnitudes of the eigenvectors are unified). Maximal and minimal magnitude vectors are plotted  
50  
51 as the direction arrays of maximum and minimum compression in Figure 6 a-b, based on [68-  
52  
53 69]. Because of the nature of deviatoric strain, the minimum of three eigenvalues is negative,  
54  
55 while the maximum is positive, indicating compression and tension, respectively.  
56  
57  
58  
59  
60  
61  
62  
63  
64  
65

#### 4. Discussion

In order to determine the reason behind the observed peak broadening, the diffraction patterns along one transect on the map (Figure 4a) have been analyzed in greater depth. In this region, peak broadening of the  $(0\bar{1}3)$  peak derives from striking of the peak (Figure 4 b - d). Along this transect, only one dislocation direction is seen in the deep bulk. The increase in strain coincides with onset of a second activated dislocation system, indicated by the beginning of second peak streaking directions (Figure 4c). A third dislocation direction appears in the zone of large strain and maximum peak broadening, with side peaks arising, which indicates subgrain formation (Figure 4d). A plateau, shown in Figure 3b, is achieved once additional slip systems are activated, and after this system comes to saturation, the further dislocation increase leads to further broadening (i.e. peak width increase). For instance, at least 3 subgrains with similar but distinct orientations were indexed within one of the measurement spots located in the near-surface bulk zone. The misorientation between the two neighboring grains has been found to be about  $21.6^\circ$ , with the rotation axis roughly along the  $[011]$  axis of the first one of them. The orientation of the third one is found to be even closer to the orientation of the first one (with a tiny misorientation of only  $1.1^\circ$  between them), while the rotation axis is along the  $[10\bar{1}]$  direction of the first one. The first and third grain come from the same initial grain (the third one being a subgrain of the first one, with almost identical orientation), while the second one is an entirely newly-formed grain. A change in crystal orientation (Figure 2c) arises there where the subgrain occurs, and coincides with the end of peak width plateau, i.e. the onset of further peak broadening (Figure 3 a-b). This may be achieved when the dislocation density limit (maximum) is reached in one slip system and an additional slip system is activated, as indicated by additional peak striking observed in Figure 4 c-d. Peak broadening is caused by plastic deformation that

1  
2  
3  
4 subsequently induces subgrain formation near the surface. The appearance of subgrains with  
5  
6 orientations that do not match the bulk steel may be interpreted as parts of the bulk  
7  
8 transformation due to interpenetration of the oxide and bulk steel layers. This means that the  
9  
10 near-interface bulk area is not entirely a single crystal.  
11  
12  
13  
14

15 In order to exclude the possible contribution of polishing to plastic deformation, an  
16  
17 additional  $\mu$ XRD scan was performed on a second sample of the same material, polished but not  
18  
19 treated in LBE. After polishing, but before annealing, the sample consists of smaller-size grains.  
20  
21  $\mu$ XRD scanning showed there is no significant contribution from polishing: even if there was any  
22  
23 strain induced by polishing, the annealing effect in the beginning of exposure to LBE eliminates  
24  
25 that strain. Besides that, maximum peak width values are only 1/3 of maximum values after  
26  
27 exposure to 800 °C LBE, even if there were no reduction due to the annealing (Figures 7 a-b).  
28  
29  
30  
31  
32  
33  
34  
35

36 The experimental data suggest a significant plastic strain in the ALK sample to about a  
37  
38 10-15  $\mu$ m depth from the interface with the oxide layer, which implies a substantial source of  
39  
40 deformation other than the expected effects occurring due to oxidation at the ALK/LBE initial  
41  
42 interface. We considered two possible hypotheses that may explain these findings. One  
43  
44 hypothesis is based on the internal oxidation within the metal, in the region near the oxide/metal  
45  
46 interface. Internal oxidation is observed in bcc-Fe alloys containing Al and Cr [44], and so Al  
47  
48 and Cr would be the candidates for oxidation, with  $\text{Al} \rightarrow \text{Al}_2\text{O}_3$  being the thermodynamically  
49  
50 most favorable phase. We calculated the amount of strain that could be produced by oxidation of  
51  
52 the available Al, and estimated the depth to which such oxidation could occur based on diffusion  
53  
54 from the interface. The partial molar volumes of Al and Cr in ALK were computed using the  
55  
56 Thermo-Calc TCFE7 database [27]. We assumed a Fe-Cr-Al composition of 83 : 13 : 4 wt%,  
57  
58  
59  
60  
61  
62  
63  
64  
65

1  
2  
3  
4 kept at 800 °C for 360 hours. The grain size was assumed to be large enough that only bulk  
5  
6 diffusion of oxygen was relevant, i.e., neglecting grain boundary diffusion. Oxygen at the initial  
7  
8 ALK/LBE interface was assumed to be in local equilibrium with LBE, which contained  $5 \times 10^{-6}$   
9  
10 wt% O based on our oxygen sensor reading. Another issue with this assumptions is that if a  
11  
12 passivating alumina layer formed, the oxygen at the interface would no longer be expected to be  
13  
14 in equilibrium with the LBE. Bulk diffusion of O was based on data for pure Fe, and at 800°C it  
15  
16 was taken to be  $D_O = 3.2 \times 10^{-8}$  m<sup>2</sup>/s [44]. The rate of the oxidation reaction was assumed to be  
17  
18 fast enough that diffusion of O was the limiting factor. Diffusion of Al was ignored since the  
19  
20 diffusion rate of Al in Fe is much slower than that of O in Fe. Volumes and thermal expansion  
21  
22 coefficients of Al<sub>2</sub>O<sub>3</sub> [9] and Cr<sub>2</sub>O<sub>3</sub> [10] were taken from literature data. If all of the locally  
23  
24 available Al were oxidized, we found that the volume increase of the ALK would be 4.5%. The  
25  
26 equivalent linear strain would be 1.5%, already quite large. Cr is more abundant in ALK, and has  
27  
28 a somewhat larger volume increase on oxidation. If all the locally available Cr were oxidized the  
29  
30 volume increase of the sample would be ~ 20%. Clearly, internal oxidation could lead to  
31  
32 substantial plastic strain.  
33  
34  
35  
36  
37  
38  
39  
40

41 We calculated the potential depth of oxidation, assuming complete oxidation of Al only,  
42  
43 and that at each point in time, all Al to a depth  $x(t)$  is oxidized, while none of the Al beyond is.  
44  
45 We assumed the O concentration profile to be linear, equal to the fixed value at the interface, and  
46  
47 zero at  $x(t)$ . We accounted only for the oxygen transport required to oxidize the Al. The oxygen  
48  
49 transport to maintain the linear concentration profile is much smaller, and was ignored. Setting  
50  
51 the infinitesimal amount of O required to oxidize Al over a depth  $dx$  and area  $A$  with the amount  
52  
53 transported over a time period  $dt$  gives an integral equation for  $x(t)$ ,  
54  
55  
56  
57  
58  
59  
60  
61  
62  
63  
64  
65

$$\frac{3}{2} c_*^{Al} A dx = AD \frac{c_*^O}{x} dt \quad (4.1)$$

$$x dx = \frac{2}{3} \frac{c_*^O}{c_*^{Al}} D dt = \frac{2}{3} \frac{c_0^O}{c_0^{Al}} D dt \quad (4.2)$$

Solving this gives the result:

$$x^2 = \frac{4}{3} \frac{c_0^O}{c_0^{Al}} D t. \quad (4.3)$$

Here  $D$  is the diffusion coefficient for O,  $c_0^O$  is the atomic fraction of oxygen in the ALK at the interface,  $c_0^{Al}$  is the atomic fraction of Al in the ALK (before oxidation),  $c_*^O = c_0^O \rho$  is the O atoms per unit volume in ALK at the interface,  $c_*^{Al} = c_0^{Al} \rho$  is the Al atoms per unit volume, and  $\rho$  is the total atoms per unit volume of ALK. Substituting in the assumed values, at  $t = 360$  h,  $x = 39 \mu\text{m}$ . This suggests that internal oxidation is a plausible candidate for the source of plastic strain that reaches 10-15  $\mu\text{m}$  deep into the ALK. Al-oxide growth/formation may cause the striking and splitting of the grain structure in the near-surface bulk zone, by a plate (wall) formation, might be illustrated as ‘driving a wedge into wood’.

The other hypothesis is that strain is induced by the temperature change (cooling) at the end of the static corrosion tests in LBE. The strain was calculated for ALK in LBE at 800°C, supposing that the only oxides on the steel surface are  $\text{Al}_2\text{O}_3$  and  $\text{Fe}_3\text{O}_4$  (as the most dominant oxide species determined elsewhere [19]). The thermal expansion coefficient is temperature-dependent and for the three materials taken into account here (alumina, magnetite, and ALK steel) it is represented by a sigmoidal function [10] as a function of temperature. The strain in each material in the defined temperature range is given by:

$$\varepsilon = \int_{298K}^{1073K} \alpha(T) dT \quad (4.4)$$

where  $\alpha(T)$  is the linear thermal expansion coefficient. The integral has been solved geometrically, as the calculated surface below the sigmoidal function. The calculated strain values for  $\text{Al}_2\text{O}_3$ ,  $\text{Fe}_3\text{O}_4$  and ALK steel in the defined temperature range ( $25^\circ\text{C} - 800^\circ\text{C}$ ) are:

$$\varepsilon_{\text{Al}_2\text{O}_3} = 775 \cdot 8.4 \cdot 10^{-6} = 0.65 \% \quad (4.5)$$

$$\varepsilon_{\text{ALK}} = 775 \cdot 14.2 \cdot 10^{-6} = 1.1 \% \quad (4.6)$$

$$\varepsilon_{\text{Fe}_3\text{O}_4} = 775 \cdot 16.4 \cdot 10^{-6} = 1.3 \% \quad (4.7)$$

We get a rough assessment of the resulting strain on/near the bulk-oxide interface as a consequence of thermal expansion: If  $\text{Fe}_3\text{O}_4$  is the only oxide in the scale atop the steel surface,  $\varepsilon_{\text{Fe}_3\text{O}_4} > \varepsilon_{\text{ALK}}$ , and hence the resulting strain is:

$$\varepsilon_{\text{Fe}_3\text{O}_4} - \varepsilon_{\text{ALK}} = 2.2 \cdot 775 \cdot 10^{-6} = 0.17 \% \quad (4.8)$$

However, if  $\text{Al}_2\text{O}_3$  is the only oxide in the scale, we have  $\varepsilon_{\text{Al}_2\text{O}_3} < \varepsilon_{\text{ALK}}$ , so the resulting strain is:

$$\varepsilon_{\text{Al}_2\text{O}_3} - \varepsilon_{\text{ALK}} = -5.8 \cdot 775 \cdot 10^{-6} = -0.45 \% \quad (4.9)$$

A positive value means that there is a tension in the oxide and compression in the bulk, and vice versa. Evidently, the contribution from the thermal expansion mismatch is not negligible, but the values are far below our measurements and the computed values when using the internal oxidation assumption. However, in all likelihood the strain found may be a combination of both internal oxidation and thermal expansion. In case of mixed oxide, or multi-layer scale (as it is the real case, at least in this study), the contribution of resulting strains,  $A = (\varepsilon_{\text{Fe}_3\text{O}_4} - \varepsilon_{\text{ALK}})$  and  $B = (\varepsilon_{\text{Al}_2\text{O}_3} - \varepsilon_{\text{ALK}})$  has to be weighted (keeping in mind the different signs of the values in Eq. 4.8 and 4.9) to calculate the total resulting strain,  $\varepsilon_{\text{tot}}$ :

$$\varepsilon_{\text{tot}} = xA + (1-x)B$$

1  
2  
3  
4 where x is an assessed percentage of magnetite in scale, based on EDS analysis results.  
5  
6

## 7 **5. Conclusions**

10 1) Plastic deformation (dislocations induced) and sub-grain formation in the near-interface bulk  
11 zone were observed.  
12  
13

14 2) Dislocation density calculated from crystal mis-orientation correlates well with peak width  
15 and strain distribution, indicating that strain in the lattice mainly comes from plastic deformation  
16  
17  
18

19 3) Grain refinement (rotation/tilting) of the bulk crystal structure (lattice) causes changing in  
20 crystal orientation in the near-interface region, and could be caused by internal oxidation, which  
21 subsequently induces strain due to the oxide and bulk crystal lattices misfit  
22  
23  
24  
25  
26  
27

28 4) We considered two possible origins of the strain induced in the bulk: one is the internal  
29 oxidation of aluminum through the diffusion of oxygen from LBE into bulk, while the other one  
30 is the thermal expansion mismatch between the oxide and the bulk. According to the results  
31 presented here, it is plausible that internal oxidation is the more dominant mechanism of strain  
32 induction.  
33  
34  
35  
36  
37  
38  
39  
40  
41  
42  
43  
44

## 45 **Acknowledgements**

46 This work is supported by the U.S. Department of Energy (DOE) SunShot program (Award No. DE-  
47 EE0005941), the National Natural Science Foundation of China (Grant No. 51671154 and 51405507), the  
48 National Key Research and Development Program of China (Grant No. 2016YFB0700404) and the  
49 National Basic Research Program of China (“973” Program) (Grant No. 2015CB057400). The authors  
50 thank Dr. Alan Bolind for some very helpful editing and improvement of the text, and Dr. Martin Kunz  
51 from the Experimental systems group at LBNL for technical assistance during the experiment. K.C. also  
52  
53  
54  
55  
56  
57  
58  
59  
60  
61  
62  
63  
64  
65

1  
2  
3  
4 appreciates the supports from the open project of State Key Laboratory for Mechanical Behavior of  
5  
6 Materials (Grant No. 20171907), and from the International Joint Laboratory for Micro/Nano  
7  
8 Manufacturing and Measurement Technologies and the Collaborative Innovation Center of High-End  
9  
10 Manufacturing Equipment. The ALS is supported by the Director, Office of Science, Office of Basic  
11  
12 Energy Sciences, Materials Science Division, of the U.S. Department of Energy under Contract No. DE-  
13  
14 AC02-05CH11231 at LBNL.  
15  
16  
17

## 18 **References**

- 20  
21 [1] OECD – NEA 7268, Handbook on Lead-bismuth Eutectic Alloy and Lead Properties,  
22  
23 Materials Compatibility, Thermal- hydraulics and Technologies, 2015 Edition  
24  
25 (<https://www.oecd-nea.org/science/pubs/2015/7268-lead-bismuth-2015.pdf>).  
26  
27  
28 [2] C. Schroer, J. Konys, Physical Chemistry of Corrosion and Oxygen Control in Liquid Lead  
29  
30 and Lead-Bismuth Eutectic, Forschungszentrum Karlsruhe (Wissenschaftliche Berichte FZKA  
31  
32 7364), 2007. ([https://www.deutsche-digitale-](https://www.deutsche-digitale-bibliothek.de/binary/UXLSJBDAKUYFBCOB6OENDWQCLUZX4Y24/full/1.pdf)  
33  
34 [bibliothek.de/binary/UXLSJBDAKUYFBCOB6OENDWQCLUZX4Y24/full/1.pdf](https://www.deutsche-digitale-bibliothek.de/binary/UXLSJBDAKUYFBCOB6OENDWQCLUZX4Y24/full/1.pdf))  
35  
36  
37 [3] D. Frazer, E. Stergar, C. Cionea, P. Hosemann, Liquid Metal as a Heat Transport Fluid for  
38  
39 Thermal Solar Power Applications, Energy Procedia 49 (2014), 627–636.  
40  
41 <http://www.sciencedirect.com/science/article/pii/S1876610214005220>  
42  
43  
44 [4] S. Khericha, E. Loewen, Nucl. Eng. Des. 241 (2011), Lead Coolant Test Facility—Design  
45  
46 concept and requirements, 3008–3016.  
47  
48 <http://www.sciencedirect.com/science/article/pii/S0029549311004869>  
49  
50  
51 [5] K. L. Murty, I. Charit, J. Nucl. Mater. 383 (2008), Structural materials for Gen-IV nuclear  
52  
53 reactors: challenges and opportunities, 189–195.  
54  
55 <http://www.sciencedirect.com/science/article/pii/S0022311508004960>  
56  
57  
58  
59  
60  
61  
62  
63  
64  
65

- 1  
2  
3  
4 [6] H. Aït Abderrahim, P. Baeten, D. De Bruyn, J. Heyse, P. Schuurmans, J. Wagemans,  
5  
6 MYRRHA, a Multipurpose hybrid research reactor for high-energy applications, Nucl. Phys.  
7  
8 News 20 (2010) 24–28. <http://www.tandfonline.com/doi/abs/10.1080/10506890903178913>  
9  
10  
11 [7] J. Wallenius, ELECTRA-FCC: a centre for Generation IV system research and training, In:  
12  
13 ELECTRA workshop presentations, Stockholm, Sweden 2012, KTH.  
14  
15  
16 [8] M. Wohlmuther, W. Wagner, PIE preparation of the MEGAPIE target, J. Nucl. Mater. 431  
17  
18 (2012), 10-15. <http://www.sciencedirect.com/science/article/pii/S0022311511009767>  
19  
20  
21 [9] G.K. White, M.L. Minges, Thermophysical properties of some key solids: An update, Int. J.  
22  
23 Thermophys., 18 (1997) 1269-1327.  
24  
25  
26 [10] Subvolume D ‘Non-Tetrahedrally Bonded Binary Compounds II’ of Volume 41  
27  
28 ‘Semiconductors’ of Landolt-Börnstein - Group III Condensed Matter, Springer, Berlin, 2001.  
29  
30  
31 [11] J. Zhang, N. Li, Review of the studies on fundamental issues in LBE corrosion, J. Nucl.  
32  
33 Mater. 373 (2008), 351–377.  
34  
35  
36 <http://www.sciencedirect.com/science/article/pii/S0022311507008422>  
37  
38 [12] A.L. Johnson, D. Parsons, J. Manzerova, D. L Perry, D. Koury, B. Hosterman, J.W. Farley,  
39  
40 Spectroscopic and microscopic investigation of the corrosion of 316/316L stainless steel by lead-  
41  
42 bismuth eutectic (LBE) at elevated temperatures: importance of surface preparation, J. Nucl.  
43  
44 Mater. 328 (2004), 88–96. <http://www.sciencedirect.com/science/article/pii/S0022311504001102>  
45  
46  
47 [13] P. Hosemann, D. Frazer, E. Stergar and K. Lambrinou, Twin boundary-accelerated  
48  
49 ferritization of austenitic stainless steels in liquid lead–bismuth eutectic, Scr. Mater. 118 (2016),  
50  
51 37-40. <http://www.sciencedirect.com/science/article/pii/S1359646216300732>  
52  
53  
54  
55  
56  
57  
58  
59  
60  
61  
62  
63  
64  
65

- 1  
2  
3  
4 [14] M. de Caro, K. Woloshun, F. Rubio, S.A. Maloy, P. Hosemann, Heavy Liquid Metal  
5 Corrosion of Structural Materials in Advanced Nuclear Systems, JOM 65 (2013) 1057–1066.  
6  
7 <https://link.springer.com/article/10.1007/s11837-013-0663-7>  
8  
9  
10  
11 [15] J. Abella, A. Verdager, S. Colominas, K. Ginestar, L. Martinelli, Fundamental data:  
12 solubility of nickel and oxygen and diffusivity of iron and oxygen in molten LBE, J. Nucl. Mat.  
13  
14 415 (2011) 329–337. <http://www.sciencedirect.com/science/article/pii/S0022311511003953>  
15  
16  
17 [16] J. Zhang, A review of steel corrosion by liquid lead and lead– bismuth, Corros. Sci. 51  
18  
19 (2009) 1207–1227. <http://www.sciencedirect.com/science/article/pii/S0010938X09000936>  
20  
21  
22 [17] N. Li, Active control of oxygen in molten lead-bismuth eutectic systems to prevent steel  
23  
24 corrosion and coolant contamination, J. Nucl. Mater. 300 (2002) 73-81  
25  
26 <http://www.sciencedirect.com/science/article/pii/S0022311501007139>  
27  
28  
29 [18] J. Zhang, Oxygen control technology in applications of liquid lead and lead-bismuth  
30  
31 systems for mitigating materials corrosion, J. Appl. Electrochem. 43 (2013), 755-771.  
32  
33 <https://link.springer.com/article/10.1007/s10800-013-0568-8>  
34  
35  
36 [19] C. Cionea, M. D. Abad, Y. Aussat, D. Frazer, A. J. Gubser, P. Hosemann, Oxide scale  
37  
38 formation on 316L and FeCrAl steels exposed to oxygen controlled static LBE at temperatures  
39  
40 up to 800 °C, Sol. En. Mater. Sol. Cell. 144 (2016), 235-246.  
41  
42  
43 [20] L. Martinelli, F. Balbaud-Célérier, G. Picard, G. Santarini, Oxidation mechanism of an Fe–  
44  
45 9Cr–1Mo steel by liquid Pb–Bi eutectic alloy at 470 °C (Part III), Corros. Sci. (2008) 2549–  
46  
47 2559.  
48  
49 <http://www.sciencedirect.com/science/article/pii/S0010938X08002552>  
50  
51  
52 [21] L. Martinelli, F. Balbaud-Célérier, A. Terlain, S. Bosonnet, G. Picard, G. Santarini,  
53  
54 Oxidation mechanism of an Fe–9Cr–1Mo steel by liquid Pb–Bi eutectic alloy at 470 °C (Part II),  
55  
56  
57  
58  
59  
60  
61  
62  
63  
64  
65

5  
6 <http://www.sciencedirect.com/science/article/pii/S0010938X08002540>

7  
8  
9 [22] L. Martinelli, F. Balbaud-Célérier, A. Terlain, S. Delpech, G. Santarini, J. Favergeon, G.

10  
11 Moulin, M. Tabarant, G. Picard, Oxidation mechanism of an Fe–9Cr–1Mo steel by liquid Pb–Bi

12  
13 eutectic alloy at 470 °C (Part I), Corros. Sci. 50 (2008) 2523–2536.

14  
15  
16 <http://www.sciencedirect.com/science/article/pii/S0010938X08002539>

17  
18  
19 [23] B. X. He, N. Li, M. Mineev, A Kinetic Model for Corrosion and Precipitation in Non-

20  
21 Isothermal LBE Flow Loop, J. Nucl. Mater. 297 (2001), 214-219.

22  
23  
24 <http://www.sciencedirect.com/science/article/pii/S0022311501006031>

25  
26 [24] J. Zhang, P. Hosemann, S. Maloy, Models of liquid metal corrosion, J. Nucl. Mater. 404

27  
28 (2010) 82–96. <http://www.sciencedirect.com/science/article/pii/S0022311510002369>

29  
30  
31 [25] J. Zhang, Long-Term Behaviors of Oxide Layer in Liquid Lead–Bismuth Eutectic (LBE),

32  
33 Part I: Model Development and Validation, Oxid. Met. 80 (2013), 669-685.

34  
35  
36 <https://link.springer.com/article/10.1007/s11085-013-9450-7>

37  
38 [26] J. Zhang, Long-Term Behaviors of Oxide Layer in Liquid Lead–Bismuth Eutectic (LBE),

39  
40 Part II: Model Application, Oxid. Met. 81 (2014), 597-615.

41  
42  
43 <https://link.springer.com/article/10.1007/s11085-014-9469-4>

44  
45 [27] Thermo-Calc Software, TCFE7 thermodynamic database (for steels and Fe-based alloys)

46  
47  
48 [http://www.thermocalc.com/media/10306/tcfe7\\_extended\\_info\\_2013-02-07.pdf](http://www.thermocalc.com/media/10306/tcfe7_extended_info_2013-02-07.pdf)

49  
50  
51 [28] T. B. Massalski, *Binary Alloys Phase Diagrams*, The Materials Information Society,

52  
53 Materials Park (1990).

1  
2  
3  
4 [29] G. Müller, G. Schumacher, F. Zimmermann, Investigation on oxygen controlled liquid lead  
5 corrosion of surface treated steels, J. Nucl. Mater. 278 (2000), 85-95.

6  
7  
8  
9 <http://www.sciencedirect.com/science/article/pii/S0022311599002111>

10  
11 [30] V. Gorynin, G.P. Karzov, V.G. Markov, V.A. Yakovlev, Structural materials for atomic  
12 reactors with liquid metal heat-transfer agents in the form of lead or lead—Bismuth alloy, Met.  
13 Sci. Heat. Treat. 41 (1999), 384–388.

14  
15  
16  
17 <https://link.springer.com/article/10.1007%2FBF02469876?LI=true>

18  
19 [31] M. Kondo, M. Takahashi, Corrosion resistance of Si- and Al-rich steels in flowing lead–  
20 bismuth, J. Nucl. Mater. 356 (2006), 203–212.

21  
22  
23  
24 <http://www.sciencedirect.com/science/article/pii/S0022311506002613>

25  
26 [32] J. Lim, H. O. Nam, I. S. Hwang, J.-H. Kim, A study of early corrosion behaviors of FeCrAl  
27 alloys in liquid lead–bismuth eutectic environments, J. Nucl. Mater. 407 (2010), 205-210.

28  
29  
30  
31 <http://www.sciencedirect.com/science/article/pii/S0022311510005982>

32  
33 [33] A. Weisenburger, A. Jianu, S. Doyle, M. Bruns, R. Fetzer, A. Heinzl, M. Del Giacco, W.  
34 An, G. Müller, Oxide scales formed on Fe–Cr–Al-based model alloys exposed to oxygen  
35 containing molten lead, J. Nucl. Mater. 437 (2013), 282-292.

36  
37  
38  
39 <http://www.sciencedirect.com/science/article/pii/S0022311513004509>

40  
41 [34] M. Del Giacco, A. Weisenburger, A. Jianu, F. Lang, G. Mueller, Influence of composition  
42 and microstructure on the corrosion behavior of different Fe–Cr–Al alloys in molten LBE, J.  
43 Nucl. Mater. 421 (2012), 39-46.

44  
45  
46  
47 <http://www.sciencedirect.com/science/article/pii/S002231151101004X>

48  
49 [35] S. Takaya, T. Furukawa, M. Inoue, T. Fujisawa, T. Okuda, F. Abe, S. Ohnuki and A.  
50 Kimura, Corrosion resistance of Al-alloying high Cr–ODS steels in stagnant lead–bismuth, J.  
51  
52

1  
2  
3  
4 Nucl. Mater. 398 (2010) 132–138.

5  
6 <http://www.sciencedirect.com/science/article/pii/S0022311509008319>

7  
8  
9 [36] P. Tomaszewicz, G. R. Wallwork, The oxidation of high-purity iron-chromium-aluminum  
10 alloys at 800°C, Oxid. Met. 20 (1983), 75–109.

11  
12  
13 <https://link.springer.com/article/10.1007%2FBF00662042?LI=true>

14  
15  
16 [37] Z. G. Zhang, X. L. Zhang, L. Sheng, X. Teng, “The effect of the third element Cr on  
17 oxidation behavior of Fe-xCr-10Al (at.%) alloy at 900°C”, The Effect of the Third Element Cr  
18 on Oxidation Behavior of Fe-xCr-10Al (at.%) Alloys at 900 °C, Open Corr. J. 2 (2009) 37-44.

19  
20  
21  
22 <https://benthamopen.com/contents/pdf/TOCORRJ/TOCORRJ-2-37.pdf>

23  
24  
25 [38] F. H. Stott, G. C. Wood and J. Stringer, “The influence of alloying elements on the  
26 development and maintenance of protective scales”, Oxid. Met. 44 (1995), 113-145.

27  
28  
29 <https://link.springer.com/article/10.1007/BF01046725>

30  
31  
32 [39] C. Wagner, Passivity and inhibition during the oxidation of metal at elevated temperatures,  
33 Corros. Sci. 5 (1965), 751-764.

34  
35  
36 <http://www.sciencedirect.com/science/article/pii/S0010938X65800038>

37  
38  
39 [40] D. Naumenko, W. J. Quadackers, A. Galerie, Y. Wouters and S. Jourdain, Parameters  
40 affecting transient oxide formation on FeCrAl based foil and fiber materials, High Temp. 20 (3)

41  
42  
43 (2003), 287–293. <http://www.tandfonline.com/doi/abs/10.1179/mht.2003.034>

44  
45  
46 [41] R. Prescott and M. J. Graham, The formation of aluminum oxide scales on high-temperature  
47 alloys, Oxid. Met. 38 (1992), 233–254. <https://link.springer.com/article/10.1007/BF00666913>

48  
49  
50 [42] M. D. Abad, S. Parker, D. Frazer, M. Rebello de Figueiredo, A. Lupinacci, K. Kikuchi and  
51 P. Hosemann, Evaluation of the Mechanical Properties of Naturally Grown Multilayered Oxides

1  
2  
3  
4 Formed on HCM12A Using Small Scale Mechanical Testing, *Oxid. Met.* 84 (2015), 211-231.

5  
6  
7 <https://link.springer.com/article/10.1007/s11085-015-9551-6>

8  
9 [43] A. Weisenburger, A. Heinzl, G. Muller, H. Muscher, A. Rousanov, T91 cladding tubes  
10 with and without modified FeCrAlY coatings exposed in LBE at different flow, stress and  
11 temperature conditions, *J. Nucl. Mat.* 376 (2008) 274-81.

12  
13  
14  
15  
16 <http://www.sciencedirect.com/science/article/pii/S0022311508000664>

17  
18 [44] M. Auinger, V.C. Praig, B. Linder, H. Danninger, Grain boundary oxidation in iron-based  
19 alloys, investigated by <sup>18</sup>O enriched water vapour – The effect of mixed oxides in binary and  
20 ternary Fe–{Al, Cr, Mn, Si} systems, *Corrosion Sci.* 96 (2015) 133-143.

21  
22  
23  
24  
25  
26 <http://www.sciencedirect.com/science/article/pii/S0010938X15001699>

27  
28 [45] P. Hosemann, P. Dickerson, R. Dickerson, N. Li, S. A. Maloy, Transmission electron  
29 microscopy (TEM) on oxide layers formed on D9 stainless steel in lead bismuth eutectic (LBE),  
30  
31  
32  
33  
34  
35 *Corros. Sci.* 66 (2013) 196–202.

36  
37 <http://www.sciencedirect.com/science/article/pii/S0010938X12004490>

38 [46] C.-W. Yang, J.-H. Kim, R. E. Triambulo, Y.-H. Kang, J.-S. Lee, J.-W. Park, The  
39 mechanical property of the oxide scale on Fe–Cr alloy steels, *J. Alloy. Compounds* 549 (2013) 6-  
40  
41  
42  
43  
44  
45  
46  
47  
48  
49  
50  
51  
52  
53  
54  
55  
56  
57  
58  
59  
60  
61  
62  
63  
64  
65  
10. <http://www.sciencedirect.com/science/article/pii/S0925838812016362>

[47] V. K. Tolpygo, D. R. Clarke, Spalling failure of  $\alpha$ -alumina films grown by oxidation: I.  
Dependence on cooling rate and metal thickness, *Mat. Sci. Eng. A* 278, 1-2 (2000) 142-150.

<http://www.sciencedirect.com/science/article/pii/S092150939900581X>

[48] V. K. Tolpygo, D. R. Clarke, Spalling failure of  $\alpha$ -alumina films grown by oxidation: II  
Decohesion nucleation and growth, *Mat. Sci. Eng. A* 278, 1-2 (2000) 151-161.

<http://www.sciencedirect.com/science/article/pii/S0921509399005821>

- 1  
2  
3  
4 [49] C. Zhu, X. Zhao, I. S. Molchan, G. E. Thompson, G. Liang, P. Xiao, Effect of cooling rate  
5 and substrate thickness on spallation of alumina scale on Fecralloy, Mat. Sci. Eng. A 528 (2011)  
6  
7  
8  
9 8687-8693. <http://www.sciencedirect.com/science/article/pii/S0921509311009294>  
10  
11 [50] S. Wang, C. M. Harvey, B. Wang, Room temperature spallation of  $\alpha$ -alumina films grown  
12 by oxidation, Eng. Fract. Mech. 178 (2017) 401-415.  
13  
14  
15  
16 <http://www.sciencedirect.com/science/article/pii/S0013794417302448>  
17  
18 [51] C. Zhu, X. Zhao, Y. Chen, Y. Zhao, P. Xiao, I. S. Molchan, G. E. Thompson, Spallation  
19 Behaviour of Alumina Scale Formed on FeCrAlY Alloy After Isothermal Oxidation, Oxid. Met.  
20  
21  
22  
23  
24 85 (2016) 391-408. <https://link.springer.com/article/10.1007/s11085-015-9602-z>  
25  
26 [52] M. Izumi, Y. Murakami, Y. Konishi, T. Manako, M. Kawasaki, and Y. Tokura, Structure  
27 characterization and magnetic properties of oxide superlattices, Phys. Rev. B **60** (1999) 1211.  
28  
29  
30  
31 <https://journals.aps.org/prb/abstract/10.1103/PhysRevB.60.1211>  
32  
33 [53] J. H. Stout, D. A. Shores, J. G. Goedjen, M. E. Armacanqui, Stresses and cracking of oxide  
34 scales, Mat. Sci. Eng. A 120-121 (1989) 193-197.  
35  
36  
37  
38 <http://www.sciencedirect.com/science/article/pii/0921509389907399>  
39  
40 [54] T. Homma and Y. Pyun, Proc. 3rd Japan Institute of Metals Int. Symp. on High  
41 Temperature Corrosion, Trans. Jpn. Inst. Met. Suppl., (1983), p. 161  
42  
43  
44 [55] M. Kunz, N. Tamura, K. Chen, A. A. MacDowell, R. S. Celestre, M. M. Church, S. Fakra,  
45  
46  
47  
48  
49  
50  
51  
52  
53  
54  
55  
56  
57  
58  
59  
60  
61  
62  
63  
64  
65

1  
2  
3  
4 [56] M. Kunz, K. Chen, N. Tamura, H.-R. Wenk, Evidence for residual elastic strain in deformed  
5 natural quartz, *Am. Mineral.* 94 (2009) 1059–1062.

6  
7  
8  
9 <https://www.degruyter.com/view/j/ammin.2009.94.issue-7/am.2009.3216/am.2009.3216.xml>

10  
11 [57] N. Tamura, in: *Strain Dislocation Gradients from Diffraction. Spatially-Resolved Local*  
12 *Structure and Defects*, edited by R. Barabash and G. Ice, London, 2014 (pp. 125–155).

13  
14  
15  
16 [https://books.google.com/books?hl=en&lr=&id=S9G6CgAAQBAJ&oi=fnd&pg=PR5&dq=N.+Tamura,+in:+Strain+Dislocation+Gradients+from+Diffraction.+Spatially-Resolved+Local+Structure+and+Defects,+edited+by+R.+Barabash+and+G.+Ice+\(World+Scientific,+London,+2014\),+pp.+125%E2%80%93155&ots=r5QVTQUMjG&sig=5igPgxH2YEtvJiALiVieUpnalo#v=onepage&q&f=false](https://books.google.com/books?hl=en&lr=&id=S9G6CgAAQBAJ&oi=fnd&pg=PR5&dq=N.+Tamura,+in:+Strain+Dislocation+Gradients+from+Diffraction.+Spatially-Resolved+Local+Structure+and+Defects,+edited+by+R.+Barabash+and+G.+Ice+(World+Scientific,+London,+2014),+pp.+125%E2%80%93155&ots=r5QVTQUMjG&sig=5igPgxH2YEtvJiALiVieUpnalo#v=onepage&q&f=false)

17  
18  
19  
20  
21  
22  
23  
24 [58] K. Chen, N. Tamura, W. Tang, M. Kunz, Y. C. Chou, K. N. Tu, and Y. S. Lai, High  
25 precision thermal stress study on flip chips by synchrotron polychromatic x-ray microdiffraction,  
26 *J. Appl. Phys.* 107 (2010) 063502. <http://aip.scitation.org/doi/abs/10.1063/1.3309750>

27  
28  
29  
30  
31 [59] K. Chen, M. Kunz, N. Tamura, and H.-R. Wenk, Residual stress preserved in quartz from  
32 the San Andreas Fault Observatory at Depth, *Geology* 43 (2015), 219.

33  
34  
35  
36  
37  
38  
39  
40 <https://pubs.geoscienceworld.org/geology/article-lookup/43/3/219>

41  
42  
43 [60] A. Lupinacci, K. Chen, Y. Li, M. Kunz, Z. Jiao, G. S. Was, M. D. Abad, A. M. Minor, P.  
44 Hosemann, Characterization of ion beam irradiated 304 stainless steel utilizing nanoindentation  
45 and Laue microdiffraction, *J. Nucl. Mater.* 458 (2015), 70.

46  
47  
48  
49  
50  
51 <http://www.sciencedirect.com/science/article/pii/S0022311514008411>

52  
53 [61] Dan Qian, Anfeng Zhang, Jianxue Zhu, Yao Li, Wenxin Zhu, Baolu Qi, Nobumichi  
54 Tamura, Dichen Li, Zhongxiao Song, Kai Chen, Hardness and microstructural inhomogeneity at  
55  
56  
57  
58  
59  
60  
61  
62  
63  
64  
65

1  
2  
3  
4 the epitaxial interface of laser 3D-printed Ni-based superalloy, Applied Physics Letters, 109,  
5  
6 101907, DOI: 10.1063/1.4962485, 2016. <http://aip.scitation.org/doi/abs/10.1063/1.4962485>  
7  
8  
9 [62] Y. Li, L. Wan and K. Chen, A look-up table based approach to characterize crystal twinning  
10  
11 for synchrotron X-ray Laue microdiffraction scans, J. Appl. Crystallogr., 48 (2015), 747-757  
12  
13 DOI: 10.1107/S1600576715004896 (<http://scripts.iucr.org/cgi-bin/paper?nb5143> )  
14  
15  
16 [63] R. I. Barabash, G. E. Ice, Quantitative analysis of dislocation arrangements induced by  
17  
18 electromigration in a passivated Al (0.5 wt% Cu)Al (0.5 wt% Cu) interconnect, J. Appl.  
19  
20 Phys. 93 (2003) 5701. <http://aip.scitation.org/doi/abs/10.1063/1.1563033>  
21  
22  
23 [64] R. Maaß , S. Van Petegem, D. Grolimund, H. Van Swygenhoven, D. Kiener, G. Dehm,  
24  
25 Crystal rotation in Cu single crystal micropillars: In situ Laue and electron backscatter  
26  
27 diffraction, Appl. Phys. Lett. 92 (2008) 071905.  
28  
29 <http://aip.scitation.org/doi/pdf/10.1063/1.2884688>  
30  
31  
32 [65] B. C. Valek, N. Tamura, R. Spolenak, W. A. Caldwell, A. A. MacDowell, R. S. Celestre, H.  
33  
34 A. Padmore, J. C. Bravman, B. W. Batterman, W. D. Nix, and J. R. Patel, Early stage of plastic  
35  
36 deformation in thin films undergoing electromigration, J. Appl. Phys. 94 (2003), 3757.  
37  
38 <http://aip.scitation.org/doi/abs/10.1063/1.1600843>  
39  
40  
41 [66] J. S. Chung, G. E. Ice, Automated indexing for texture and strain measurement with broad-  
42  
43 bandpass x-ray microbeams, J. Appl. Phys. 86 (1999), 5249-5255.  
44  
45  
46 <http://aip.scitation.org/doi/abs/10.1063/1.371507>  
47  
48  
49 [67] G. Zhou, W. Zhu, H. Shen, Y. Li, A. Zhang, N. Tamura, K. Chen, Real-time microstructure  
50  
51 imaging by Laue microdiffraction: A sample application in laser 3D printed Ni-based  
52  
53 superalloys, Scientific Reports 6 (2016), 28144.  
54  
55  
56 <https://www.ncbi.nlm.nih.gov/pmc/articles/PMC4908403/>  
57  
58  
59  
60  
61  
62  
63  
64  
65

- 1  
2  
3  
4 [68] Y. Li, D. Qian, J. Xue, J. Wan, A. Zhang, N. Tamura, Z. Song, and K. Chen, A synchrotron  
5  
6 study of defect and strain inhomogeneity in laser-assisted three-dimensionally-printed Ni-based  
7  
8 superalloy, *Appl. Phys. Lett.* 107 (2015), 181902; doi: 10.1063/1.4934839  
9  
10 (<http://aip.scitation.org/doi/10.1063/1.4934839> )  
11  
12  
13  
14 [69] K. Chen, M. Kunz, Y. Li, E. Zepeda-Alarcon, M. Sintubin, and H.-R. Wenk, Compressional  
15  
16 residual stress in Bastogne boudins revealed by synchrotron X-ray microdiffraction, *Geophys.*  
17  
18 *Res. Lett.*, 43 (2016) 6178–6185  
19  
20 (<http://onlinelibrary.wiley.com/doi/10.1002/2016GL069236/abstract>)  
21  
22 doi:10.1002/2016GL069236  
23  
24  
25 [70] G. E. Ice and R. I. Barabash, “White Beam Microdiffraction and Dislocations Gradients”,  
26  
27 *Dislocation in Solids*, Chapter 79, Vol. 13 (2007) 499-601. [https://doi.org/10.1016/S1572-](https://doi.org/10.1016/S1572-4859(07)80011-8)  
28  
29 [4859\(07\)80011-8](https://doi.org/10.1016/S1572-4859(07)80011-8)  
30  
31  
32  
33 [71] Alkrothal 720 (ALK) datasheets: resistance heating wire and resistance wire (updated on  
34  
35 2017-01-19 at 11:22 AM), and strip (updated on 2017-12-06 at 10:51 AM).  
36  
37 <https://www.kanthal.com/en/products/material-datasheets/?query=Alkrothal&sort=>  
38  
39  
40 [72] B. Joseph, M. Picat, F. Barbier, “Liquid metal embrittlement: A state-of-the-art appraisal”,  
41  
42 *Eur. Phys. J. AP* 5 (1999) 19–31. <https://doi.org/10.1051/epjap:1999108>  
43  
44  
45 [73] T. Sample, H. Kolbe, “Liquid metal embrittlement (LME) susceptibility of the 8–9% Cr  
46  
47 martensitic steels F82H-mod., OPTIFER IVb and their simulated welded structures in liquid Pb–  
48  
49 17Li”, *J. Nucl. Mater.* 283–287 (2000) 1336–1340. [https://doi.org/10.1016/S0022-3115\(00\)00097-0](https://doi.org/10.1016/S0022-3115(00)00097-0)  
50  
51  
52 [74] C. F. Old, “Liquid metal embrittlement of nuclear materials”, *J. Nucl. Mater.* 92 (1980) 2–  
53  
54  
55 25. [https://doi.org/10.1016/0022-3115\(80\)90136-1](https://doi.org/10.1016/0022-3115(80)90136-1)  
56  
57  
58  
59  
60  
61  
62  
63  
64  
65

1  
2  
3  
4 [75] J. Van den Bosch, P. Hosemann, A. Almazouzi, S. A. Maloy, “Liquid metal embrittlement  
5 of silicon enriched steel for nuclear applications”, J. Nucl. Mater. 398 (2010) 116–121.  
6  
7

8  
9 <https://doi.org/10.1016/j.jnucmat.2009.10.020>  
10

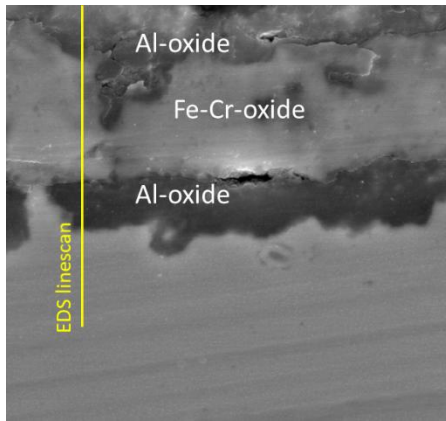
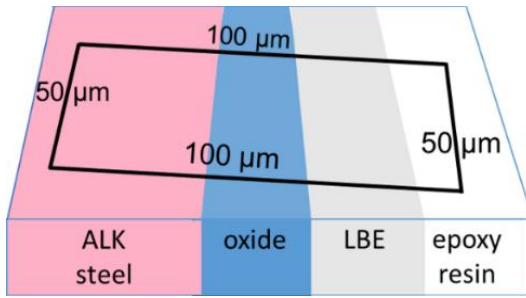
11 [76] B. Long, Z. Tong, F. Gröschel, Y. Dai, “Liquid Pb–Bi embrittlement effects on the T91  
12 steel after different heat treatments”, J. Nucl. Mater. 377, 1 (2008) 219–224.  
13

14  
15 <https://doi.org/10.1016/j.jnucmat.2008.02.050>  
16  
17  
18  
19  
20  
21  
22  
23  
24  
25  
26  
27  
28  
29  
30  
31  
32  
33  
34  
35  
36  
37  
38  
39  
40  
41  
42  
43  
44  
45  
46  
47  
48  
49  
50  
51  
52  
53  
54  
55  
56  
57  
58  
59  
60  
61  
62  
63  
64  
65

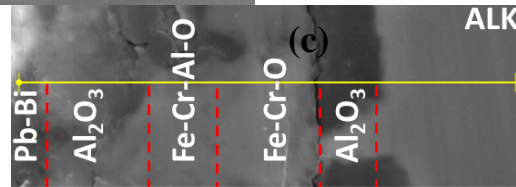
**A study of deformation and strain induced in bulk by the oxide layers  
formation on a Fe-Cr-Al alloy in high-temperature liquid Pb-Bi eutectic**

M. P. Popovic et al.

(Figures)

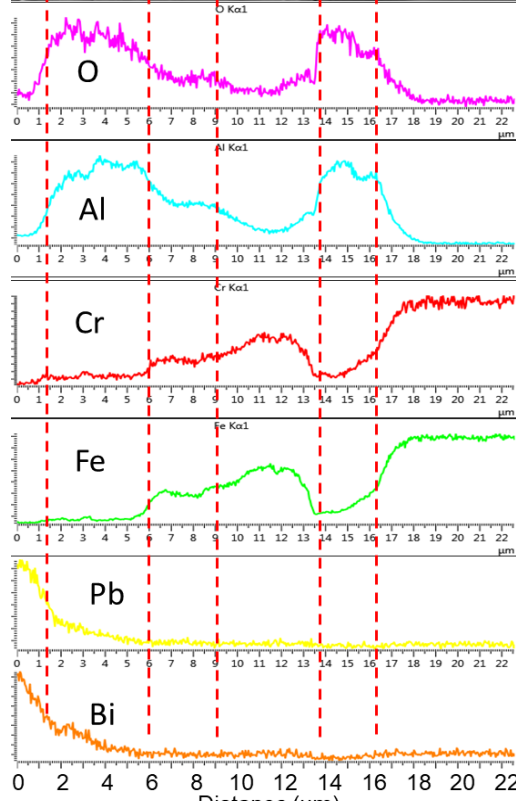


(a)

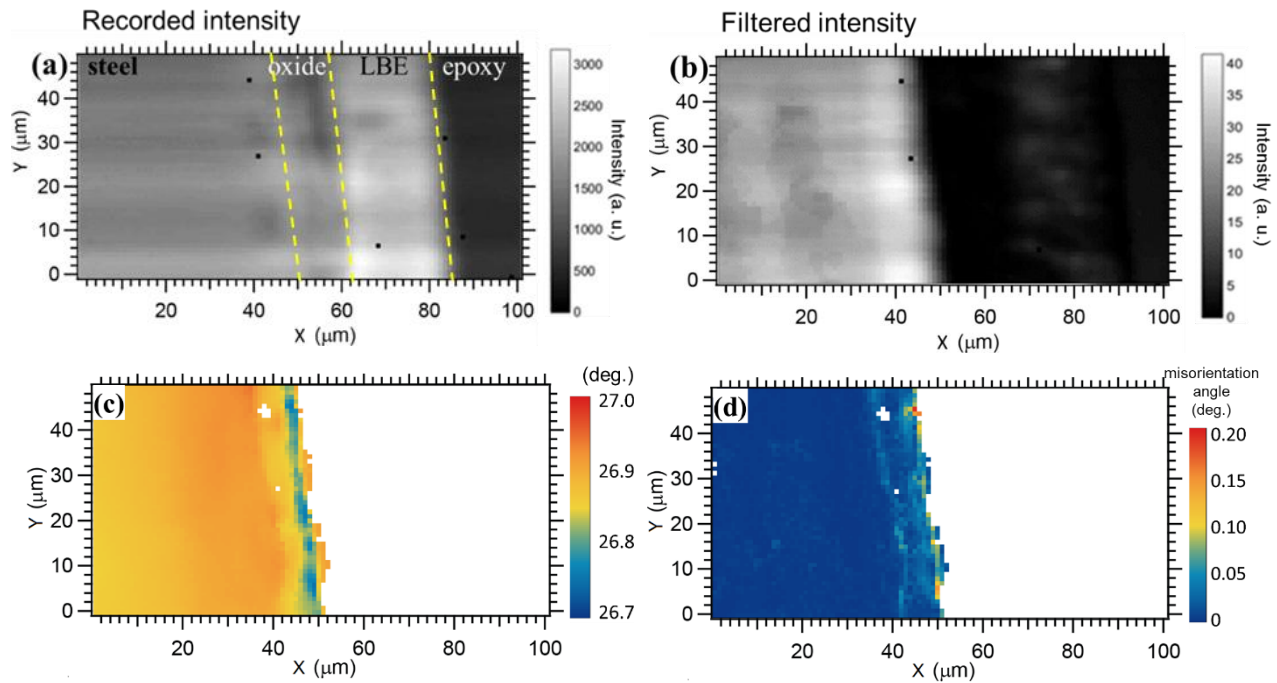


(c)

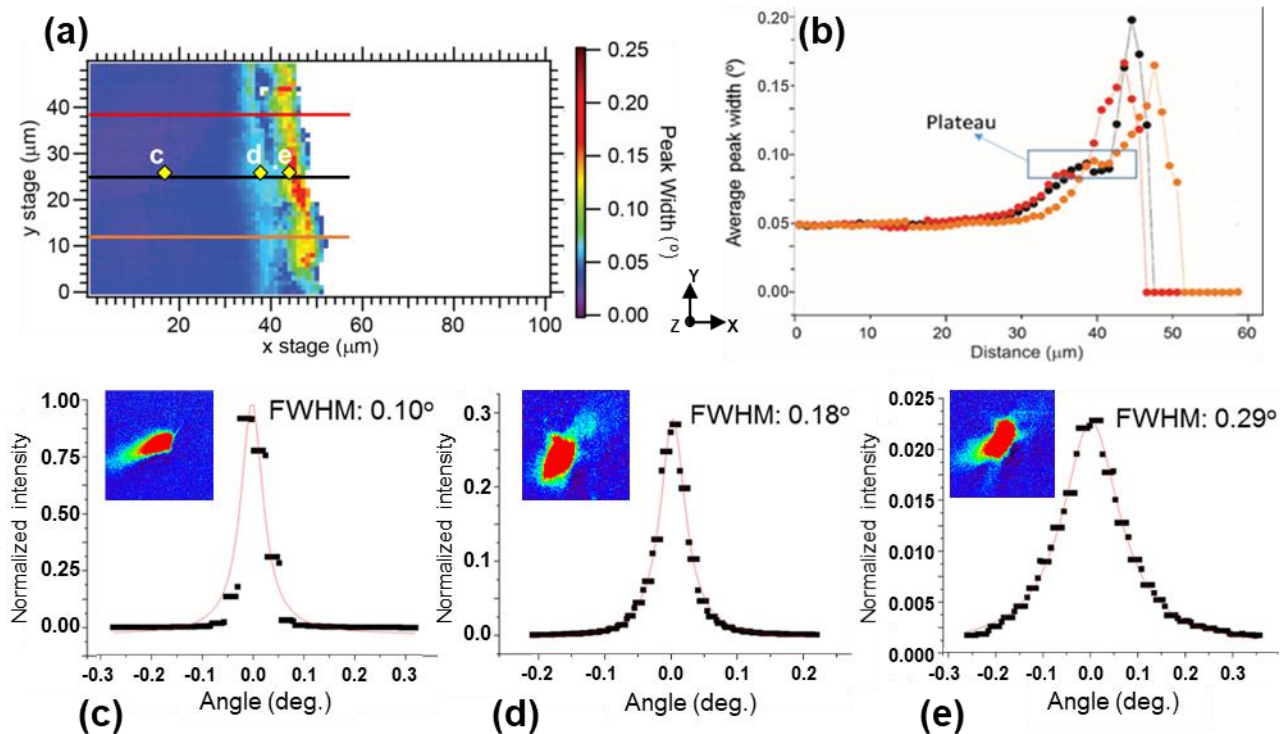
(b)



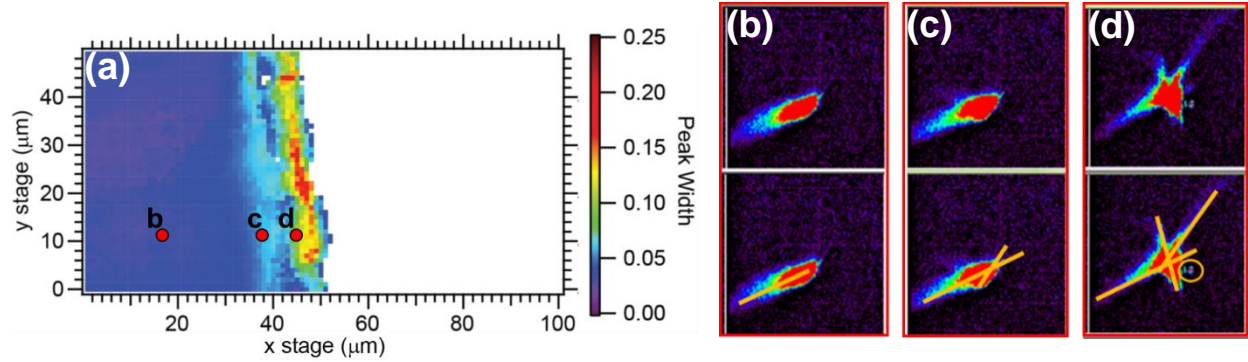
**Figure 1.** (a) Laue-XRD analyzed spot ( $100 \times 50 \mu\text{m}^2$  rectangle) covering near-interface steel bulk, oxide layer grown on steel, and LBE residues over the oxide, as seen in perspective. The black box represents the XRD-scanned area; (b) SEM cross-section image of the oxide layers grown on ALK steel sample in exposure to Pb-Bi eutectic (LBE) at  $800^\circ\text{C}$ ; (c) EDS line scan of the oxide layers grown on tested ALK steel sample.



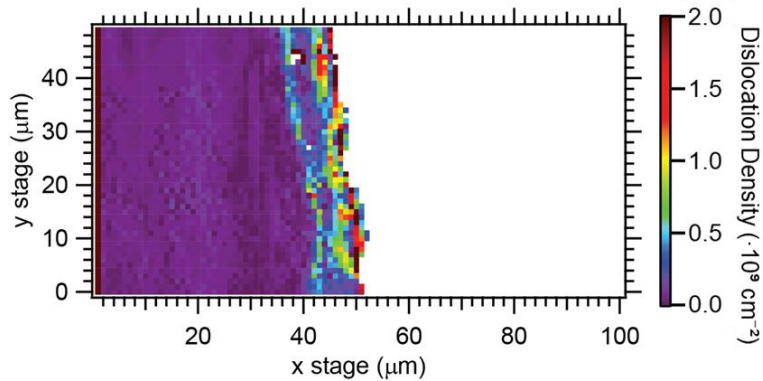
**Figure 2.** (a) Recorded-intensity map (average intensity of the diffraction peaks); (b) Filtered-intensity map displaying spots with more than 6 peaks identifying BCC steel; (c) bulk crystal orientation map of [001] direction in a narrow angle range ( $26.7^{\circ}$ - $27.0^{\circ}$ ); (d) lattice misorientation map, obtained as the difference (subtraction) between the values of the neighboring pixels in image (c): two “belts” of a sudden drop/jump in orientation changes are visible near the bulk/oxide interface, indicating the formation of the sub-grains in that region.



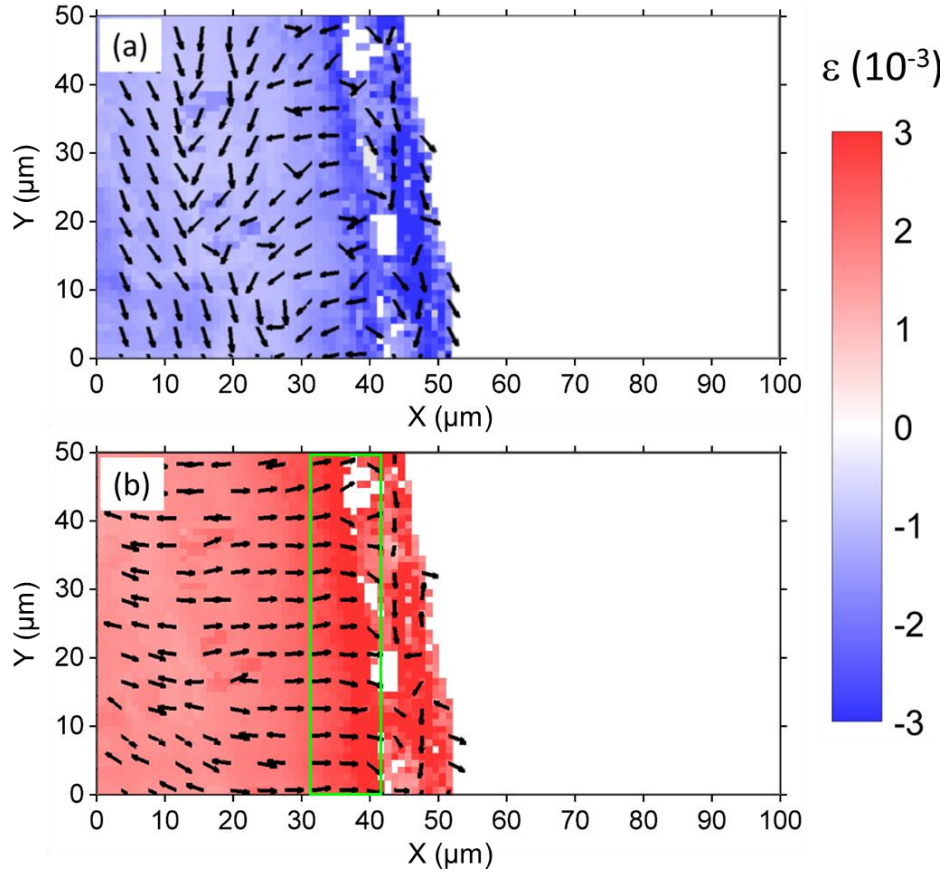
**Figure 3.** (a) Average peak width distribution of the scanned area; (b) Average peak width evolution along the patterns (three lines parallel to the X-axis on Figure 3a); (c-e) Broadening of the  $(0\bar{1}3)$  Laue peak width in three arbitrarily chosen spots corresponding to the yellow dots on Figure 3a: plotted in 2D projection along the most broadened direction (top), and in topographic projections (bottom). Peak width measured by fitting the intensity with Lorentzian distribution function.



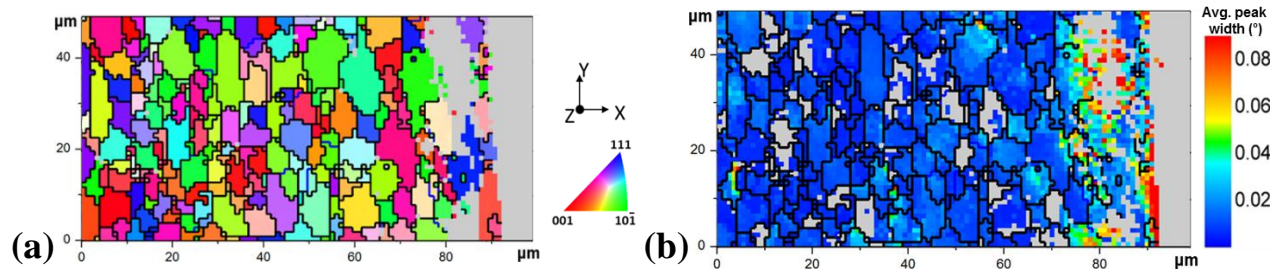
**Figure 4.** (a) Average peak width distribution, and (b-d) Streaking of the  $(0\bar{1}3)$  peak in more than one direction, as moving along the direction parallel to the X-axis, from the deep bulk towards the steel-oxide interface (corresponding to the spots b - d, respectively, labeled on fig. 4a). (b) Only one dislocation direction in deep bulk. (c) Increase of strain coincides with second dislocation direction and the beginning of peak broadening. (d) Large strain and peak width, with three directions of dislocation. Side peaks forming (circled spot on fig. 4d) indicate a new grain formation.



**Figure 5.** Dislocation density map of the XRD-scanned area.

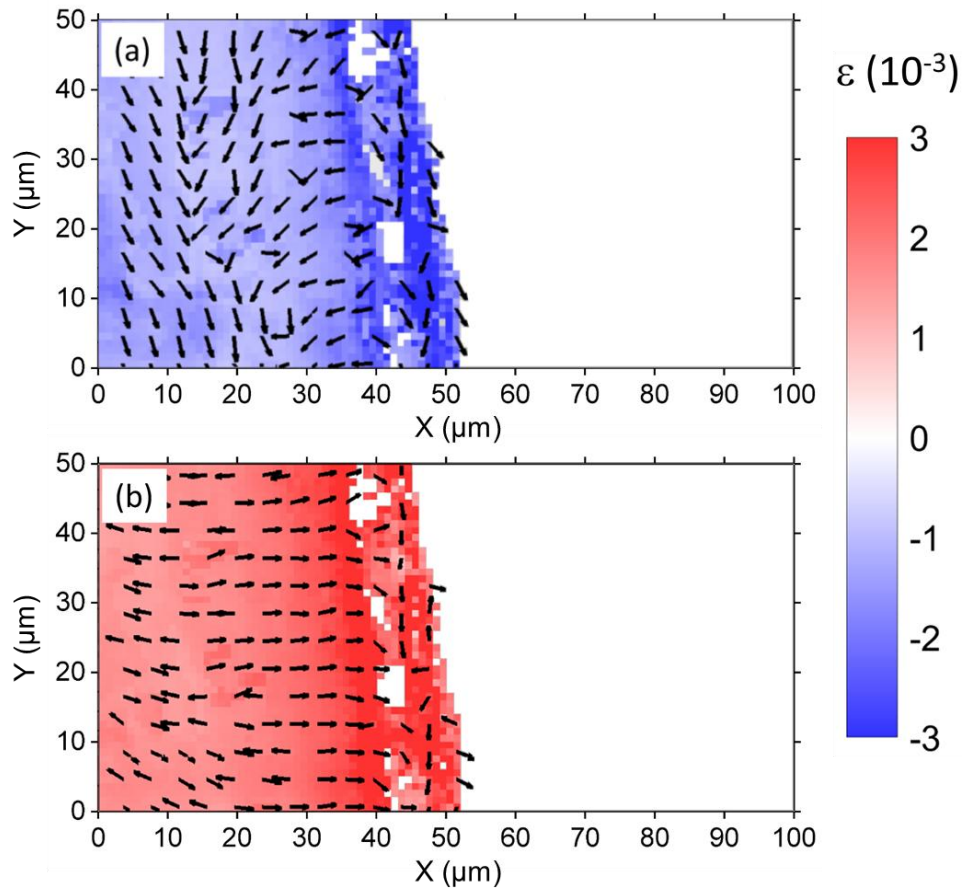


**Figure 6.** (a) Compressive principal strain and (b) tensile principal strain in bulk (next to the oxide scale). Projections of the principal strain axes on the X-Y plane are denoted by arrows in every third pixel. A zone in the bulk next to the steel-oxide interface suffers compression (due to both thermal expansion mismatch and internal oxidation), while below that zone there is a compensatory (reactive/consequent) tension maximum (green rectangle in Figure 6b).



**Figure 7.** (a) In-plane orientation map in X-direction and (b) peak width distribution map of an ALK sample polished only but without treatment in LBE.

## GRAPHICAL ABSTRACT



Compressive (top) and tensile (bottom) principal strain distribution in the  $\mu$ XRD-analyzed ferritic Fe-Cr-Al alloy material, in the bulk next to the alloy/oxide interface (arrows denote projections of the principal strain axes on X-Y plane).